









Publication Year	2018
Acceptance in OA @INAF	2020-09-29T09:58:40Z
Title	Far-ultraviolet Activity Levels of F, G, K, and M Dwarf Exoplanet Host Stars
Authors	France, Kevin; Arulanantham, Nicole; Fossati, Luca; LANZA, Antonino Francesco; Loyd, R. O. Parke; et al.
DOI	10.3847/1538-4365/aae1a3
Handle	http://hdl.handle.net/20.500.12386/27516
Journal	THE ASTROPHYSICAL JOURNAL SUPPLEMENT SERIES
Number	239



Far-ultraviolet Activity Levels of F, G, K, and M Dwarf Exoplanet Host Stars*

Kevin France¹ , Nicole Arulanantham¹ , Luca Fossati² , Antonino F. Lanza³ , R. O. Parke Loyd⁴ , Seth Redfield⁵ , and P. Christian Schneider⁶

¹Laboratory for Atmospheric and Space Physics, University of Colorado, 600 UCB, Boulder, CO 80309; USA; kevin.france@colorado.edu

²Space Research Institute, Austrian Academy of Sciences, Schmiedlstrasse 6, A-8042 Graz, Austria

³INAF—Osservatorio Astrofisico di Catania, Via S. Sofia, 78, I-95123 Catania, Italy

⁴School of Earth and Space Exploration, Interplanetary Initiative, Arizona State University, Tempe, AZ, USA

⁵Astronomy Department and Van Vleck Observatory, Wesleyan University, Middletown, CT 06459-0123, USA

⁶Hamburger Sternwarte, Gojenbergsweg 112, D-21029 Hamburg, Germany

Received 2018 July 8; revised 2018 September 10; accepted 2018 September 12; published 2018 November 16

Abstract

We present a survey of far-ultraviolet (FUV; 1150–1450 Å) emission line spectra from 71 planet-hosting and 33 non-planet-hosting F, G, K, and M dwarfs with the goals of characterizing their range of FUV activity levels, calibrating the FUV activity level to the 90–360 Å extreme-ultraviolet (EUV) stellar flux, and investigating the potential for FUV emission lines to probe star–planet interactions (SPIs). We build this emission line sample from a combination of new and archival observations with the *Hubble Space Telescope*-COS and -STIS instruments, targeting the chromospheric and transition region emission lines of Si III, NV, C II, and Si IV. We find that the exoplanet host stars, on average, display factors of 5–10 lower UV activity levels compared with the non-planet-hosting sample; this is explained by a combination of observational and astrophysical biases in the selection of stars for radial-velocity planet searches. We demonstrate that UV activity–rotation relation in the full F – M star sample is characterized by a power-law decline (with index $\alpha \approx -1.1$), starting at rotation periods $\gtrsim 3.5$ days. Using NV or Si IV spectra and knowledge of the star’s bolometric flux, we present a new analytic relationship to estimate the intrinsic stellar EUV irradiance in the 90–360 Å band with an accuracy of roughly a factor of ≈ 2 . Finally, we study the correlation between SPI strength and UV activity in the context of a principal component analysis that controls for the sample biases. We find that SPIs are not a statistically significant contributor to the observed UV activity levels.

Key words: planetary systems – stars: activity – stars: low-mass

1. Introduction

The success of planet searches employing radial velocity techniques and transit photometry has demonstrated that ~ 300 – 400 stars in the solar neighborhood ($d < 50$ pc) host confirmed planetary systems. *TESS* will expand this list dramatically in the next several years. With so many planets now discovered, the next step toward the study of “comparative planetology” is the characterization of the physical processes that shape these worlds. Of particular interest are the environmental parameters that control the physical and chemical state of potentially inhabited rocky planets around cool stars (M–F dwarfs; $T_{\text{eff}} \approx 2500$ – 6000 K). These include the high-energy photon and particle environment (Segura et al. 2010; Tilley et al. 2017), as well as the potential for stellar and planetary magnetospheres to interact (Garraffo et al. 2016). These “exoplanet space weather” effects may ultimately control the habitability of these systems (e.g., Airapetian et al. 2017). NASA and ESA are currently studying design reference missions for the detection and/or spectroscopic characterization of potentially habitable rocky planets (e.g., Rauer et al. 2014; France et al. 2016a; Mennesson et al. 2016; Roberge & Luvoir Mission Concept Team 2017). However, rocky planets around M dwarfs will likely be the only potentially habitable planets whose atmospheres can be probed for signs of life (with

JWST and ELTs) prior to a Large UVOIR mission in the 2030s–2040s (Deming et al. 2009; Belu et al. 2011; Snellen et al. 2015). We need to characterize the radiation and magnetic environments of our stellar neighbors so that spectroscopic observations of their planets can be confidently interpreted.

1.1. The Importance of the Host Star

It is now clear that the planetary effective surface temperature alone is insufficient to characterize the habitable zone (HZ) and accurately interpret atmospheric gases with a potentially biological origin. The UV stellar spectrum is required to understand HZ atmospheres, as it both drives and regulates atmospheric heating and chemistry on Earth-like planets and is critical to the long-term stability of terrestrial atmospheres. Our quest to discover and characterize biological signatures on rocky planets must consider the star–planet system as a whole, including the interaction between the stellar photons, particles, and the exoplanetary atmosphere. The dependence of abiotic formation of “biomarker” molecules (e.g., O₂, O₃, CH₄, and CO₂) on the stellar far- and near-UV irradiance (approximately 912–1700 Å and 1700–3200 Å respectively), particularly around M dwarfs, has been well-documented (e.g., Hu et al. 2012; Tian et al. 2014; Harman et al. 2015; Shields et al. 2016).

In addition, the long-term stability of the atmospheres of rocky planets is driven by the ionizing radiation and particle output of their host stars. Atmospheric escape is a key factor shaping the evolution and distribution of low-mass planets (e.g., Lopez & Fortney 2013; Owen & Wu 2013) and their

* Based on observations made with the NASA/ESA *Hubble Space Telescope*, obtained from the data archive at the Space Telescope Science Institute. STScI is operated by the Association of Universities for Research in Astronomy, Inc. under NASA contract NAS 5-26555.

habitability (Lammer et al. 2009; Cockell et al. 2016). Extreme-UV (EUV; $100 \lesssim \lambda \lesssim 911 \text{ \AA}$) photons from the central star drive thermospheric heating, and this may lead to significant atmospheric escape (Vidal-Madjar et al. 2003; Tian et al. 2008; Murray-Clay et al. 2009; Bourrier & Lecavelier des Etangs 2013; Ehrenreich et al. 2015; Spake et al. 2018). Ionization by EUV photons and the subsequent loss of atmospheric ions to stellar wind pick-up can also drive extensive atmospheric mass-loss on geologic timescales (e.g., Rahmati et al. 2014 and references therein). Stellar far-ultraviolet (FUV) observations serve as a means for predicting the ionizing (extreme-UV) flux from cool stars, either through the use of solar scaling relations (Linsky et al. 2014; Youngblood et al. 2016) or more detailed differential emission measure techniques (e.g., Loudén et al. 2017).

1.2. Exoplanetary Magnetic Fields and Star–Planet Interactions (SPIs)

A planet and its host star may interact in many ways, with most studies focusing on their photon+particle, gravitational, and magnetic field interactions (e.g., Cuntz et al. 2000). A central question for a planet’s ability to retain an atmosphere is “what is the role of magnetic fields?” (Adams 2011; do Nascimento et al. 2016). Searches for exoplanetary magnetic fields have not yielded any firm detections to date (Grießmeier 2015). Magnetic fields play a crucial role in protecting surface life from damaging high-energy particles from stellar winds and coronal mass ejections (Lammer et al. 2012), as well as promoting the long-term stability of planetary atmospheres (Tian 2015). In the solar system, Earth is the only “habitable zone” rocky planet (roughly comprising Venus, Earth, and Mars) that was able to retain its water and the only planet out of the three that has a substantial magnetic field today.

Magnetic SPIs have drawn the interest of the community because they might provide a way to detect and measure planetary magnetic fields (e.g., Vidotto et al. 2010; Cauley et al. 2015; Lanza 2015; Rogers 2017). The presence of a planetary magnetic field may induce interactions that can generate planetary radio emission (Zarka 2007; Ignace et al. 2010; Vidotto et al. 2012), early-ingress NUV light curves (Fossati et al. 2010; Vidotto et al. 2010; Cauley et al. 2015), enhanced flare activity (Pillitteri et al. 2015), and FUV aurorae (Yelle 2004; Menager et al. 2013). Radio emission from these systems remains inconclusive (Bastian et al. 2018), and NUV light curve interpretations are debated (Turner et al. 2016a, 2016b). Close-in giant planets are predicted to have substantial magnetic field strengths (Christensen et al. 2009), however, auroral emission from exoplanets has not been conclusively detected so far (e.g., Bastian et al. 2000; Lazio et al. 2004; France et al. 2010; Hallinan et al. 2013; Lecavelier des Etangs et al. 2013; Kruczek et al. 2017). Enhanced flare activity in favorable star–planet systems (Lanza 2018) appears promising and phase-resolved observations may provide more direct clues to the properties of exoplanetary magnetism.

Exoplanetary magnetic fields may be indirectly observable by the influence they produce on their host stars, one possible form of the oft searched for stellar SPIs (e.g., Shkolnik et al. 2003, 2005; Lanza 2008, 2013; Shkolnik & Llama 2017). The magnitude of this SPI, as measured by the energy dissipated in the stellar atmosphere, should depend on the strength of the stellar magnetic field, the planetary magnetic field, and the relative speed of the planet’s orbital velocity compared to the

stellar magnetic rotation rate (Lanza 2012). While this technique does not provide a direct measure of the planetary magnetic field strength, it does allow for both the detection of exoplanetary magnetic fields and their influence on their host stars.

Tidal (gravitational) SPIs may alter the rotational evolution of the host star and the orbital evolution of the planet (Poppenhaeger & Wolk 2014). In this way, tides may significantly affect the stellar activity level. This phenomenon should be particularly efficient for massive late-type stars, where the convective layers driving the stellar activity are thin and thus more easily affected by tides induced from the planet. Pillitteri et al. (2014) and Fossati et al. (2018) concluded that this is the case for the WASP-18 system, which contains a massive $\approx 10 M_J$ planet orbiting a mid-F-type star with a period of ≈ 1 day. X-ray and far-UV observations of WASP-18 indicate that the star has an anomalously low activity level for its young age, which Pillitteri et al. (2014) argued is driven by the tidal forces induced by the massive planet disrupting the α - Ω hydromagnetic dynamo in the host star.

Using data from the MUSCLES survey of planet-hosting M dwarfs (France et al. 2016a; Loyd et al. 2016; Youngblood et al. 2016), we recently presented a tentative detection of stellar SPI (France et al. 2016a). Because magnetic field strength increases with planetary mass in the solar system, one may expect that the most massive, closest-in planets in exoplanetary systems produce the largest signal on their host stars, therefore SPI signals could be expected to correlate with $M_{\text{plan}}/a_{\text{plan}}$ (or other proportionalities between the dissipated power and the star–planet system configuration; see Section 4.2), where M_{plan} is the planetary mass and a_{plan} is the semimajor axis (see, e.g., Miller et al. 2015). The MUSCLES database allowed us to explore SPI as a function of emission line formation temperature. Probing different temperature regimes was critical for the tentative detection of SPI in MUSCLES (described below), and can be used to constrain the possible location of magnetic field line reconnection and subsequent location of the plasma heating. France et al. (2016a) suggested that the systems with close-in, massive planets may indeed be generating enhanced transition region activity, as probed by $\sim (0.3\text{--}2) \times 10^5$ K gas. Conversely, no correlations with the cooler gas emitting in the lower-chromosphere were observed (traced by Mg II and Si II, $T_{\text{form}} \lesssim 10^4$ K).

However, the small sample size and low significance of the MUSCLES result ($\approx 2\text{-}\sigma$) compelled us to develop a larger sample with broader spectral type coverage. Expanding the observational basis for understanding the environmental drivers of exoplanet atmospheres and refining the SPI study were the primary motivations for assembling the large sample of exoplanet host stars and non-planet-hosting control group presented in this work.

1.3. A Survey of the Chromospheric and Transition Region Activity of Exoplanet Host Stars

In this paper, we present a new far-UV emission line survey of exoplanet host stars, including all of the available archival data from *HST*-STIS and COS (spectra from *IUE* are largely too low-quality for this work; France et al. 2016b). We acquired new *HST*-COS observations of 45 host stars, and have assembled the largest UV spectroscopic exoplanet host star and non-planet-hosting control sample to date (Tables 1 and 2). For simplicity, we refer to stars without known planetary systems

Table 1
Stellar Properties of Planet Hosts

Name	SpT	V	$B - V$	T_{eff} (K)	R_* (R_{\odot})	d (pc)	M_{planet} (M_{\oplus})	a_{planet} (au)	P_{rot} (days)
HD 120136	F7V	4.49	0.49	6310 (1)	1.33 (2)	15.6	1860	0.046	3.3 (3)
HD 197037	F7V	6.813	0.497	6150 (4)	1.15 ^a	32.3	256.6	2.07	19.1 (4)
HD 136118	F7V	6.94	0.52	6003 (5)	1.58 (5)	52.0	13300	1.45	12.2 (5)
HD 9826	F9V	4.1	0.54	6210 (2)	1.63 (2)	13.5	7494	2.55	12 (6)
HD 10647	F9V	5.52	0.551	6039 (1)	1.1 (7)	17.4	294	2.02	10 (8)
HD 23079	F9V	7.11	0.57	5848 (1)	1.13 (7)	33.2	779	1.596	19.1 ^b
HD 155358	G0V	7.28	0.545	5900 (4)	1.39 (9)	44.1	260	0.63	35.2 ^b
ρ CrB	G0V	5.39	0.612	5627 (10)	1.362 (10)	17.2	338	0.23	18.5 (10)
HD 39091	G0V	5.67	0.58	5888 (1)	2.1 ^a	18.3	3206	3.3	33.9 ^b
HD 187085	G0V	7.21	0.57	6075 (11)	1.15 ^a	44.0	255	2.0	11.4 ^b
HD 106252	G0V	7.36	0.64	5750 (1)	1.09 (7)	37.8	10500	2.7	22.8 (5)
HD 209458	G0V	7.63	0.58	6090 (12)	1.20 (13)	48.9	220	0.05	14.4 (14)
HD 114729 A	G0V	6.69	0.62	5662 (1)	1.46 (7)	36.1	300	2.1	32.3 ^b
HD 13931	G0V	7.6	0.637	5900 (16)	1.17 (16)	44.2	598	5.15	4.7 ^b
47 UMa	G1V	5.04	0.62	5892 (15)	1.24 (15)	14.1	809	2.1	24 (5)
HD 10180	G1V	7.32	0.63	5911 (17)	1.11 ^a	39.0	64.4	3.4	24 (17)
HD 117618	G2V	7.17	0.603	5855 (18)	1.19 (7)	38.0	56.1	0.17	18.9 ^b
HD 121504	G2V	7.54	0.593	6075 (1)	1.096 ^a	45.1	388	0.33	8.6 (19)
μ Ara	G3V	5.15	0.7	5800 (20)	1.245 ^a	15.5	555	1.5	31 (20)
16 Cyg B	G3V	6.2	0.66	5770 (21)	0.98 (2)	21.2	534	1.68	29.1 (22)
HD 1461	G3V	6.6	0.674	5765 (23)	1.095 (23)	23.2	7.6	0.06	29 (24)
HD 38529	G4V	5.924	0.773	5600 (25)	2.82 (25)	42.4	255	0.13	35.7 (25)
HD 37124	G4IV-V	7.68	0.667	5763 (27)	0.82 ^a	33.7	214	0.5	25 (26)
HD 147513	G5V	5.376	0.644	5700 (1)	1.0 ^a	12.8	385	1.3	4.7 (19)
HD 222582	G5V	7.69	0.65	5662 (1)	1.15 (7)	41.8	2425	1.3	25.4 ^b
HD 28185	G5V	7.81	0.71	5705 (28)	1.03 (7)	42.3	1842	1.02	30 (28)
HD 4113	G5V	7.88	0.73	5688 (29)	1.036 ^a	44.0	524	1.3	38.3 ^b
HD 65216	G5V	7.96	0.69	5718 (27)	1.036 ^a	35.6	387	1.4	26.2 ^b
HD 178911 B	G5V	7.98	0.73	5667 (7)	1.14 (7)	42.6	2317	0.3	29.7 ^b
HD 79498	G5V	8.02	0.706	5740 (4)	1.036 ^a	46.1	428	3.1	26.2 ^b
HIP 91258	G5V	8.65	0.01	5519 (30)	1.036 ^a	44.9	339	0.06	24 (30)
HD 90156	G5V	6.92	0.683	5599 (31)	1.036 ^a	22.4	18	0.2	26 (31)
HD 115617	G6.5V	4.74	0.7	5530 (7)	0.94 (7)	8.6	18.2	0.2	29 (32)
HD 70642	G6V	7.17	0.692	5670 (1)	0.97 (27)	28.1	607	3.2	142 ^b
HD 47186	G6V	7.63	0.73	5675 (33)	1.017 ^a	39.6	22.6	0.05	33 (33)
HD 92788	G6V	7.3	0.694	5754 (34)	1.05 (34)	32.3	1133	0.95	31.7 (34)
HD 102117	G6V	7.47	0.721	5672 (35)	1.27 (7)	39.7	54	0.15	34 (35)
HD 4208	G7V	7.78	0.664	5571 (1)	0.85 ^a	32.4	257	1.7	0 (7)
HD 10700	G8V	3.5	0.72	5340 (36)	0.793 (36)	3.7	3.94	0.538	34 (36)
HD 69830	G8V	5.95	0.79	5385 (37)	0.895 ^a	12.5	10	0.08	41.2 ^b
55 Cnc	G8V	5.95	0.87	5200 (38)	0.943 (38)	12.3	1230	5.4	42 (34)
HD 1237	G8V	6.578	0.757	5417 (39)	0.9 ^a	17.5	1070	0.49	10.4 (39)
HD 154345	G8V	6.74	0.76	5468 (40)	0.94 (40)	18.6	304	4.2	31 (40)
GJ 86	G9V	6.17	0.77	5350 (41)	0.855 ^a	10.8	1272	0.1	30 (42)
HD 147018	G9V	8.3	0.763	5441 (43)	0.96 ^a	43.0	2080	1.9	31.1 ^b
HD 164922	G9V	7.01	0.799	5293 (10)	0.999 (10)	22.1	114	2.1	44 (45)
HD 189733	K0V+M4V	7.648	0.93	4880 (2)	0.805 (2)	19.8	363	0.03	13.4 (47)
HD 7924	K0.5V	7.185	0.826	5177 (46)	0.78 (46)	16.8	8.7	0.06	38 (46)
HD 3651	K0.5V	5.88	0.83	5270 (16)	0.88 (48)	11.1	73.3	0.295	37 (49)
HD 128621	K1V	1.33	0.88	5336 (50)	0.863 (50)	1.25	1.1	0.04	36.2 (50)
HD 114783	K1V	7.56	0.93	5105 (1)	0.78 (7)	20.5	351	1.2	45.4 ^b
HD 97658	K1V	7.714	0.855	5050 (51)	0.908 (51)	21.1	6.4	0.08	38.5 (51)
HD 40307	K2.5V	7.147	0.95	4750 (51)	0.856 (51)	12.9	9.5	0.132	48 (51)
HD 192263	K2.5V	7.767	0.957	4965 (1)	0.75 (7)	19.3	203	0.2	24.5 (52)
ϵ Eri	K2V	3.73	0.88	4900 (51)	0.882 (51)	3.2	400	3.4	11.7 (51)
HD 192310	K2V	5.723	0.907	5166 (53)	0.8 (27)	8.8	16.9	0.3	47.67 (53)
HD 99492	K2V	7.53	1.024	4740 (54)	0.96 (54)	18.0	33.7	0.1	45 (54)
HD 128311	K3V	7.446	0.995	4965 (7)	0.73 (7)	16.5	463	1.1	14 (26)
HD 104067	K3V	7.921	0.976	4969 (55)	0.856 ^a	21.1	59	0.3	34.7 (55)
HD 156668	K3V	8.42	1.01	4850 (56)	0.72 (56)	24.5	4.2	0.05	51.5 (56)
HAT P 11	K4V	9.47	1.19	4780 (57)	0.75 (57)	37.9	26.2	0.053	30.5 (58)
WASP 69	K5V	9.87	1.06	4720 (59)	0.813 (59)	50	83	0.05	23.07 (59)
HD 85512	K6V	7.651	1.18	4300 (51)	0.778 (51)	11.2	3.5	0.26	47.1 (51)

Table 1
(Continued)

Name	SpT	V	$B - V$	T_{eff} (K)	R_* (R_{\odot})	d (pc)	M_{planet} (M_{\oplus})	a_{planet} (au)	P_{rot} (days)
GJ 832	M1.5V	8.672	1.5	3816 (51)	0.631 (51)	4.9	203	3.6	40 (51)
GJ 667 C	M1.5V	10.22	1.57	3440 (51)	0.562 (51)	6.9	5.7	0.049	105 (51)
GJ 3470	M2V	12.332	1.168	3600 (44)	0.550 (44)	29.3	13.9	0.04	...
GJ 176	M2.5V	9.951	1.54	3310 (51)	0.493 (51)	9.4	8.3	0.066	38.9 (51)
GJ 436	M3.5V	10.613	1.45	3310 (51)	0.493 (51)	10.3	23	0.03	48 (51)
GJ 1214	M4.5V	14.67	1.73	2920 (51)	0.286 (51)	14.6	6.4	0.01	53 (51)
GJ 876	M5V	10.192	1.56	3180 (51)	0.424 (51)	4.7	615	0.208	96.7 (51)
GJ 581	M5V	10.56	1.2	3310 (51)	0.493 (51)	6.3	15.9	0.04	94.2 (51)
Proxima Centauri	M5.5V	11.13	1.82	3050 (60)	0.14 (60)	1.299	1.3 (60)	0.05 (60)	83 (60)

Notes. M_{planet} and a_{planet} are for the most massive planet in each system, as listed in The Extrasolar Planets Encyclopedia. Spectral types, V , $B - V$, and distances were taken from Simbad.

^a R_* estimated based on spectral type.

^b Rotation periods are upper limits (calculated from $v \sin i$).

References. (1) Nordström et al. (2004), (2) Baines et al. (2008), (3) Baliunas et al. (1997), (4) Robertson et al. (2012), (5) Fischer et al. (2002), (6) Butler et al. (1999), (7) Valenti & Fischer (2005), (8) Marmier et al. (2013), (9) Fuhrmann & Bernkopf (2008), (10) Fulton et al. (2016), (11) Jones et al. (2006), (12) Schuler et al. (2011), (13) Brown et al. (2001), (14) Mazeh et al. (2000), (15) Fuhrmann et al. (1997), (16) Wittrock et al. (2017), (17) Lovis et al. (2011), (18) Tinney et al. (2005), (19) Mayor et al. (2004), (20) Santos et al. (2004), (21) Fuhrmann et al. (1998), (22) Hale (1994), (23) Rivera et al. (2010), (24) Wright et al. (2004), (25) Fischer et al. (2003), (26) Vogt et al. (2005), (27) Bonfanti et al. (2015), (28) Santos et al. (2001), (29) Tamuz et al. (2008), (30) Moutou et al. (2014), (31) Mordasini et al. (2011), (32) Baliunas et al. (1996), (33) Bouchy et al. (2009), (34) Fischer et al. (2001), (35) Lovis et al. (2005), (36) Tuomi et al. (2013), (37) Lovis et al. (2006), (38) von Braun et al. (2011), (39) Naef et al. (2000), (40) Wright et al. (2008), (41) Queloz et al. (1999), (42) Saar & Osten (1997), (43) Ségransan et al. (2010), (44) Bonfils et al. (2012), (45) Isaacson & Fischer (2010), (46) Howard et al. (2009), (47) Knutson et al. (2007), (48) See et al. (2017), (49) Olsperg et al. (2018), (50) DeWarf et al. (2010), (51) France et al. (2016b), (52) Henry et al. (2002), (53) Pepe et al. (2011), (54) Meschiari et al. (2011), (55) Ségransan et al. (2011), (56) Howard et al. (2011), (57) Bakos et al. (2010), (58) Sanchis-Ojeda & Winn (2011), (59) Anderson et al. (2014), (60) Anglada-Escudé et al. (2016).

as “non-planet hosts,” but acknowledge that many of these stars likely have planetary systems that have not yet been discovered (Section 2.2). We use these data to compare UV activity levels from a range of formation temperatures in the chromosphere and transition region ($T_{\text{form}} \approx 20,000\text{--}200,000$ K) in F, G, K, and M dwarfs with and without (known) planets. Using our planet-hosting sample, we examine the correlations between stellar activity and a proposed parameterization of the SPI strength ($M_{\text{plan}}/a_{\text{plan}}$). In Section 2, we describe the stellar sample, target selection process, and the new *HST* observations made in support of this work. Section 3 describes the data reduction and spectral line analysis. Section 4 presents an overview of the results on activity levels of planet hosts, a new scaling to the EUV flux from these stars, the strength of the SPI signal in the data, and numerical techniques developed to compare the UV activity to stellar and planetary parameters. We present a brief summary of this work in Section 5.

2. Stellar Targets and Observations

In order to quantify the absolute UV irradiance levels incident on orbiting planets, we require direct observations of cool stars. To date, very few stellar atmosphere codes have incorporated a complete spectral irradiance modeling that includes contributions from the chromosphere, transition region, and corona (although see, e.g., Fontenla et al. 2016). Most models, including the widely used PHEONIX (Husser et al. 2013) and Kurucz stellar atmosphere models (Castelli & Kurucz 2004), only include emission from the stellar photosphere and thus underpredict the flux below ~ 2000 Å for cool stars by orders of magnitude (Shkolnik & Barman 2014; Loyd et al. 2016).

We also wish to understand how the UV activity levels of exoplanet host stars compare with similar stars without planets.

Therefore, we have assembled a sample of known exoplanet host stars and a “control” sample without known planets (or where the presence of massive, short period planets has been ruled out; see the discussion below). Of course, *Kepler* and RV surveys have shown us that most cool stars have planets, so our “non-planet hosts” may be stars for which planets have not yet been discovered, but are possible target candidates for current and future planet discovery missions like *TESS* (Sullivan et al. 2015) and *LUVOIR* (Roberge & Luvor Mission Concept Team 2017). In practice, when we refer to “non-planet hosts,” we are referring to field stars that have been observed in previous *HST* observing programs for other primary science objectives (e.g., solar twins, the Sun in time, etc.).

In assembling this sample, we restricted ourselves to the use of observations from the broad wavelength coverage UV spectrographs on board the *Hubble Space Telescope* (STIS and COS), as this allows us to preserve a quality control threshold for wavelength and flux calibration and ensures that “optically inactive” M dwarfs are included. In the following two subsections, we briefly describe these samples.

2.1. Exoplanet Host Stars

As the original motivation for this work was the intriguing SPI signal found in the MUSCLES Treasury Survey data set (France et al. 2016a), we began assembling the list of known exoplanet host stars with archival *HST*-STIS and -COS observations. Some stars, e.g., Proxima Cen, moved from the non-planet host list to the planet host list during the course of this work (Anglada-Escudé et al. 2016). This list is also populated with stars hosting transiting planets that have been observed at UV wavelengths for absorption spectroscopy during transit (Linsky et al. 2010; Ehrenreich et al. 2012; Ben-Jaffel & Ballester 2013; Loyd et al. 2017). We note that

Table 2
Stellar Properties of Non-planet Hosts

Name	SpT	V	$B - V$	T_{eff} (K)	R_* (R_{\odot})	d (pc)	P_{rot} (days)
HD 28568	F2V	6.484	0.443	6656 (1)	1.35 (2)	41.5	0.9 (53)
HD 28033	F8V	7.35	0.51	6167 ^a	1.2 (2)	46.6	1.9 ^b
HD 33262	F9V	4.708	0.507	6158 (4)	0.96 (2)	11.6	4 (3) ^b
HD 106516	F9V	6.11	0.46	6327 (5)	1.15 ^a	22.4	...
HD 28205	G0V	7.404	0.545	6306 (6)	1.15 ^a	47.3	5.87 (6)
HD 25825	G0V	7.811	0.605	6097 (7)	1 (8)	46.9	6.5 (8)
HD 97334	G0V	6.41	0.61	5898 (9)	1.01 (3)	22.8	7.6 (10)
HD 39587	G0V	4.4	0.6	5890 (11)	0.96 (11)	8.7	5.24 (11)
HII 314	G1V	10.4	0.8	5845 (12)	0.99 (12)	130.5	1.47 (12)
16 Cyg A	G1.5V	5.95	0.64	5825 (13)	1.22 (13)	21.3	26.9 (14)
HD 72905	G1.5V	5.64	0.62	5850 (11)	0.95 (11)	14.4	4.9 (11)
HD 129333	G1.5V	7.61	0.59	5853 (15)	1 (16)	35.8	2.606 (16)
HD 199288	G2V	6.52	0.59	5757 (17)	0.969 (17)	22.1	12 (17)
α Cen A	G2V	0.01	0.71	5770 (18)	1.22 (19)	1.3	29 (20)
HD 59967	G3V	6.635	0.639	5847 (21)	0.89 (3)	21.7	6.14 (3)
HD 20630	G5V	4.85	0.67	5776 (15)	0.93 (11)	9.1	9.2 (22)
HD 43162	G6.5V	6.366	0.702	5473 (23)	0.901 (23)	16.8	7.158 (24)
HD 131156	G8V	4.593	0.777	5550 (25)	0.8 (27)	6.7	6.43 (26)
KIC 11560431	K0V	9.5	...	5094 (28)	0.892 (28)	...	3.14 (29)
HD 166	K0V	6.13	0.75	5509 (15)	0.9 (2)	13.8	6.23 (30)
HD 165341	K0V	4.03	0.86	5407 (31)	0.85 (2)	5.1	19.7 (32)
HD 103095	K1V	6.45	0.75	5033 ^a	0.93 ^a	9.1	31 (22)
HR 1925	K1V	6.23	0.84	5309 (15)	0.93 ^a	12.3	10.86 (33)
HD 22468	K2V	5.71	0.92	4867 ^a	3.9 (34)	30.7	2.84 (34)
HD 155886	K2V	5.08	0.85	4867 ^a	0.69 (35)	5.5	20.69 (36)
LTT 2050	M1V	10.331	1.507	3438 (41)	0.4 ^a	11.2	...
HD 197481	M1V	8.627	1.423	3600 (42)	0.61 (2)	9.9	4.85 (10)
Kapteyn's Star	M1V	8.853	1.58	3527 (43)	0.341 (43)	3.9	84.7 (44)
LP 415-1619	M2V	13.338	1.482	3420 (48)	0.58 (48)	46.3	...
AD Leo	M4V	9.52	1.3	3130 ^a	0.38 (2)	4.7	2.6 (10)
LHS-26	M4V	10.977	0.077	3130 ^a	0.301 (46)	5.6	87.1 (54)
Procyon	F5V	0.37	0.42	6530 (49)	2.03 (49)	3.5	10.3 (50)
EV Lac	M4V	10.26	1.59	3130 ^a	0.38 ^a	5.1	4.378 (51)
YY Gem	M0.5V	9.27	1.29	3820 (52)	0.6191 (52)	14.9 (52)	3 ^c

Notes. Spectral types, V , $B - V$, and distances were taken from Simbad.

^a R_* or T_{eff} estimated based on spectral type.

^b Rotation periods are upper limits (calculated from $v \sin i$).

^c Rotation period estimated from the age of the Castor system (Chabrier & Baraffe 1995; Torres & Ribas 2002).

References. (1) Boesgaard et al. (2016), (2) Wood et al. (2005), (3) Linsky et al. (2012b), (4) Ammler-von Eiff & Reiners (2012), (5) Ge et al. (2016), (6) Ramírez et al. (2017), (7) da Silva et al. (2015), (8) Linsky et al. (2012a), (9) Eisenbeiss et al. (2013), (10) Hempelmann et al. (1995), (11) Fichtinger et al. (2017), (12) Rice & Strassmeier (2001), (13) Booth et al. (2017), (14) Hale (1994), (15) Rich et al. (2017), (16) Berdyugina (2005), (17) Loyd & France (2014), (18) Zhao et al. (2018), (19) Kervella et al. (2003), (20) Hallam et al. (1991), (21) Reddy & Lambert (2017), (22) Brandenburg et al. (2017), (23) Gaidos & Gonzalez (2002), (24) Kajatkari et al. (2015), (25) Gray (1994), (26) Toner & Gray (1988), (27) Petit et al. (2005), (28) Brown et al. (2011), (29) Balona (2012), (30) Gaidos et al. (2000), (31) Huang et al. (2015), (32) Noyes et al. (1984), (33) Zhang (2011), (34) Fekel (1983), (35) Wood et al. (2012), (36) Donahue et al. (1996), (37) Messina et al. (2010), (38) Maldonado et al. (2017), (39) Malo et al. (2014), (40) Woolf & Wallerstein (2005), (41) Tuomi et al. (2014), (42) Pawellek et al. (2014), (43) Houdebine (2010), (44) Guinan et al. (2016), (45) Pecaut & Mamajek (2013), (46) Newton et al. (2017), (47) Kiraga (2012), (48) Mann et al. (2015), (49) Yıldız et al. (2016), (50) Arentoft et al. (2008), (51) Pettersen (1980), (52) Torres & Ribas (2002), (53) Stepien (1988), (54) Newton et al. (2016).

transits impact the observed line fluxes by less than 5% for the combined observations, therefore we do not attempt to phase-separate these data. Combining the archival observations with the 45 new exoplanet host star observations presented in Section 2.3, we have assembled 1150–1450 Å spectra of 71 stars hosting extrasolar planets.

2.2. Stars without Known Planets: “Non-planet Hosts”

We have also assembled a sample of stars with no known exoplanets to compare against the list of planet-hosting stars (see Table 2). In order to obtain medium-to-high signal-to-noise FUV spectral observations of cool stars, they must be brighter than roughly 10th magnitude in V -band ($V < 10$;

brighter for SNAP observations of solar type stars, and somewhat fainter for M dwarfs). This places the requirement that we select our sample from large RV surveys that target nearby stars (see, e.g., Valenti & Fischer 2005 and references therein). As a result, what we refer to as a “non-planet-host” really means that a planet has not been detected down to the sensitivity of these surveys. For example, the sample of 1300 FGKM stars described by Marcy et al. (2004) has a radial velocity precision to 3 m s^{-1} for FGK stars and 5 m s^{-1} for M dwarfs. This translates into a planetary mass limit of $M \sin i$ of roughly $0.1 M_{\text{Jup}}$ for planets with roughly 5–10 year orbital periods (semimajor axes $\lesssim 3 \text{ au}$). The HARPS survey has pushed to less than 1 m s^{-1} (Pepe et al. 2011), enabling the

detection of Earth-mass planets with orbital periods up to tens of days around nearby M dwarfs (Anglada-Escudé et al. 2016). It suffices to say these caveats should be kept in mind as we describe differences between the planet-hosting and non-planet-hosting samples.

The FUV observations for the bulk of the non-planet hosts were drawn from StarCat (Ayres 2010), a database of ultraviolet stellar spectra from *HST*-STIS. To prevent the omission of targets that were observed after StarCat was assembled, we cross-referenced the catalogs of Valenti & Fischer (2005), Neves et al. (2013), Buchhave & Latham (2015), and Terrien et al. (2015) with the *HST*-COS and *HST*-STIS archives. These surveys include comparisons of the metallicities of planet-hosting versus non-planet-hosting systems, so our search yielded several more stars with ultraviolet spectra that had previously been identified as non-planet hosts.

2.3. New Observations with *HST*-COS

We carried out a SNAP program with the *HST*-COS instrument (*HST* GO 14633; PI-K. France) to fill out the sample of UV activity from exoplanet host stars. We used *exoplanets.org* to assemble a list of 151 confirmed planet-hosting late F through K dwarfs within 50 pc. From these, we eliminated duplicates from the list above and applied a brightness constraint, a visual magnitude $5 < V < 8.5$, to enable robust emission line flux fitting without compromising *HST*-COS instrument safety (see Table 1).

In order to obtain a robust census of line formation temperatures in the upper atmospheres of cool stars, we selected spectral coverage from 1150 to 1450 Å. The G130M mode of COS provides the necessary wavelength coverage, the highest sensitivity of any spectral mode at these wavelengths on board *HST*, and the spectral resolution ($R \sim 16,000$) to cleanly separate and resolve the emission lines. Our *HST* SNAP observations with COS G130M provided access to a suite of spectral tracers, including neutrals: N I $\lambda 1200$ Å, C I $\lambda 1275$ Å, O I $\lambda 1304$, 1356 Å, Si I $\lambda 1425$ Å; low-ionization metals and intermediate-formation temperature species: Si III $\lambda 1206$ Å, Si II $\lambda 1260$, 1264 Å, C II $\lambda 1335$ Å; and the high formation temperature lines C III $\lambda 1175$ Å, O V $\lambda 1218$ Å, N V $\lambda 1239$, 1243 Å, Si IV $\lambda 1394$, 1403 Å. While all of these ions were present in the highest S/N observations, only C II, Si III, Si IV, and N V were detected at high significance in most of our target stars, and we consequently focus on these tracers in this work. Figures 1 and 2 display the full spectra of a sample of stars used in this work, and a zoomed-in view of the Si III emission line, respectively.

The COS G130M exposure times were between 1905 and 2020 s per star (the typical exposure time was 1920 s), in the CENWAVE 1291 setting. The total exposures were split between two focal plane offset positions (FP-POS) to mitigate both the long-term effects of Ly α gain sag on the detector and detector fixed pattern noise. The observing program executed from 2016 November 29 through 2018 February 17, with 45 out of the original 80 SNAP targets (56%) observed.

2.4. Extreme-ultraviolet Explorer Spectra

For our complete list of planet-hosting and non-planet-hosting stars, we identified 12 stars with observations in the *EUVE* archive that were considered detections by Craig et al. (1997). We assembled these data sets from the MAST *EUVE*

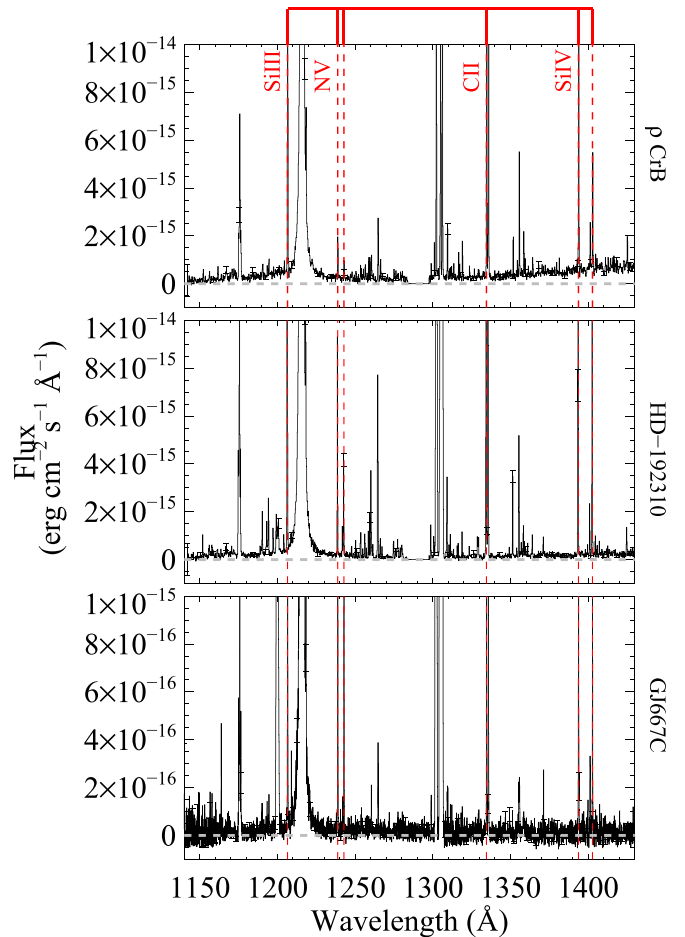


Figure 1. Example FUV exoplanet host star spectra used in this work. From top to bottom we show representative G dwarf (ρ CrB; G0V, $V = 5.39$), K dwarf (HD 192310; K2V, $V = 5.72$), and M dwarf (GJ 667 C; M2.5V, $V = 10.22$) spectra obtained with *HST*-COS G130M. Prominent hot gas lines studied here (Si III $\lambda 1206$ Å; $\log_{10} T_{\text{form}} = 4.7$, N V $\lambda 1240$ Å; $\log_{10} T_{\text{form}} = 5.2$, C II $\lambda 1335$ Å; $\log_{10} T_{\text{form}} = 4.5$, and Si IV $\lambda 1400$ Å; $\log_{10} T_{\text{form}} = 4.9$; Dere et al. 2009) are marked with red dashed lines. Strong emission lines at 1216 and 1304 Å are mainly geocoronal emission from neutral hydrogen and oxygen in Earth’s upper atmosphere.

archive, and took neutral hydrogen column densities from Linsky et al. (2014). The *EUVE* overlap sample we analyzed included: Procyon, α Cen A, χ^1 Ori, κ Cet, ξ Boo, 70 Oph, ϵ Eri, AU Mic, EV Lac, AD Leo, Proxima Cen, and YY Gem. Analysis of the *EUVE* data is presented in Section 3.2 and is presented in the context of our FUV activity survey in Section 4.1.2.

3. Analysis: Emission Line Fluxes and Bolometric Luminosities

3.1. FUV Emission Line Fluxes of Si III, N V, C II, and Si IV; 1200–1420 Å

We quantify the FUV activity level from our planet-hosting and non-planet-host samples by defining the “UV activity index,” $F_{\text{ion}}/F_{\text{bolom}}$, for the four primary ions studied in this work: Si III $\lambda 1206$ Å; $\log_{10} T_{\text{form}} = 4.7$, N V $\lambda 1240$ Å; $\log_{10} T_{\text{form}} = 5.2$, C II $\lambda 1335$ Å; $\log_{10} T_{\text{form}} = 4.5$, and Si IV $\lambda 1400$ Å; $\log_{10} T_{\text{form}} = 4.9$. The emission line luminosities, L_{ion} , are simply the wavelength-integrated fluxes scaled by the distance, $L_{\text{ion}} = 4\pi d^2 F_{\text{ion}}$, where d is the distance to the star and F_{ion} is the line

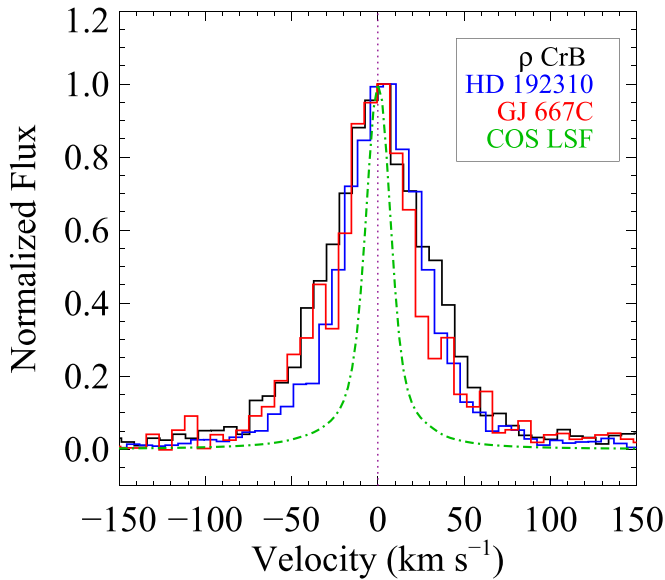


Figure 2. Spectral blow-up of the Si III λ 1206 Å ($\log_{10} T_{\text{form}} = 4.7$) upper chromospheric emission line for the three example stars shown in Figure 1 (ρ CrB: G0V, $V = 5.39$; HD 192310: K2V, $V = 5.72$; GJ 667 C: M2.5V, $V = 10.22$). The 1206 Å line-spread function of *HST*-COS is shown as the green dashed-dotted line, illustrating that the lines are spectrally resolved in all targets. The spectra have been smoothed by 3 pixels (half of an *HST*-COS spectral resolution element) for display.

flux in units of [$\text{erg cm}^{-2} \text{s}^{-1}$], described in the next paragraph. The formation temperatures are taken from the CHIANTI database (Dere et al. 2009); however, we note that different ions trace different atmospheric altitude, pressure, and temperature regimes as a function of stellar mass.

Emission line fluxes from N V (λ 1238.82 Å, λ 1242.80 Å), C II (λ 1334.53 Å, λ 1335.66 Å, λ 1335.71 Å), Si III (λ 1206.49 Å, λ 1206.55 Å, λ 1207.51 Å), and Si IV (λ 1393.75 Å, λ 1402.76 Å) were measured for both the planet-hosting and non-planet-hosting samples (see Tables 3 and 4). Since all targets are located within the Local Bubble, the dust reddening along the line of sight was assumed to be negligible. However, absorption from low-ionization gas in the local ISM, particularly in the C II λ 1334.53 Å line, can lead to systematic underestimation of the intrinsic C II emission strength (Redfield & Linsky 2004). Many of the systems had faint emission lines with low S/N, making it difficult to fit line profiles to the data. For all sources, the fluxes were calculated as

$$F_{\text{ion}} = \sum_{\lambda=\lambda_0-\delta\lambda}^{\lambda_0+\delta\lambda} \Delta\lambda F_{\lambda} - \sum_{\lambda=\lambda_0-\delta\lambda}^{\lambda_0+\delta\lambda} \Delta\lambda F_{\text{cont}}, \quad (1)$$

where $\Delta\lambda$ is the average spacing between adjacent data points (~ 0.01 Å) and F_{cont} is the flux in the continuum, estimated from a linear interpolation across the emission line. $\delta\lambda$ was set to roughly 0.5 Å, with adjustments made as needed to accommodate wider features.

L_{bolom} is the bolometric luminosity, $L_{\text{bolom}} = 4\pi d^2 F_{\text{bolom}}$. Bolometric fluxes, F_{bolom} , were calculated as

$$F_{\text{bolom}} = \sigma T_{\text{eff}}^4 \left(\frac{R_*}{d} \right)^2 \quad (2)$$

using the stellar parameters for each target (Tables 1 and 2). Although Loyd et al. (2016) measured bolometric fluxes for each of the MUSCLES stars by incorporating *HST*

spectroscopy and Tycho photometry, the simpler calculations were adopted for all objects in the survey to preserve uniformity across the sample. Comparing with the MUSCLES luminosities, we find that this simple prescription differs by as much as $\sim 30\%$ for the cooler M dwarfs (e.g., GJ 1214) and less than 10% for the warmer stars in the MUSCLES sample. Fractional luminosities, $F_{\text{ion}}/F_{\text{bolom}}$, were then obtained for each of the four measured ions by dividing the line flux by the bolometric flux.

Figures 3 and 4 display the UV activity levels as a function of the various stellar parameters studied here. Figure 3 displays the relationship between $F_{\text{Si IV}}/F_{\text{bolom}}$ and spectral slope ($\equiv B-V$) and distance. Figure 4 compares $F_{\text{Si IV}}/F_{\text{bolom}}$ and the stellar rotational period, for both the exoplanet host and non-planet-hosting samples. For stars without published rotation periods, we display upper limits based on $v \sin i$ measurements (these stars are noted with ^b in Tables 1 and 2). To avoid cluttering the body of the paper, we use Si IV as the representative example ion in this section; plots for all four ions are presented in Appendix B.

3.2. EUV Fluxes, 90–360 Å

For each *EUVE* spectrum, we converted the data to flux density units ($\text{erg cm}^{-2} \text{s}^{-1} \text{Å}^{-1}$) and integrated over the spectral region where most stars had appreciable flux (90–360 Å, or 9–36 nm). These raw integrated fluxes ($\text{erg cm}^{-2} \text{s}^{-1}$) were first background-corrected by subtracting the flux level of an *EUVE* non-detection in this band (γ Tau, $F(\text{EUV})_{\text{back}} \approx 1 \times 10^{-12} \text{ erg cm}^{-2} \text{ s}^{-1}$). YY Gem was dropped at this point because its post-subtraction integrated flux was less than 10% of the background level. The fluxes were then corrected for neutral hydrogen, neutral helium, and ionized helium attenuation by calculating optical depth spectra for the appropriate $N(\text{H I})$ from the references collated by Linsky et al. (2014). The ionization fraction of helium (0.6) and the neutral hydrogen to helium ratios (0.08) were taken from the observed local ISM values from Dupuis et al. (1995). The $N(\text{H I})$ values were necessarily low (all less than $10^{18.5}$ and 10/12 less than $10^{18.1} \text{ cm}^{-2}$; see Table 3 of Linsky et al. 2014), the ISM transmission functions are relatively linear at these wavelengths, and we calculated the average flux correction for the 90–360 Å band. These intrinsic EUV fluxes are compared with the FUV activity sample in Section 4.1.2.

4. Results: UV Activity Levels of Exoplanet Host Stars

Figure 4 shows the relationship between FUV activity index and the stellar rotation period. The stars are identified by symbol type and separated into planet versus non-planet-hosting by the use of color or black symbols, respectively. Comparing the FUV activity indices with the stellar rotation periods, we observe a “saturated” plateau followed by a roughly continuous, power-law decline in UV activity. We classify the UV activity into two rough categories: high UV-activity stars with $F_{\text{Si IV}}/F_{\text{bolom}} > 10^{-6}$ and intermediate-to-low UV-activity stars with $F_{\text{Si IV}}/F_{\text{bolom}} < 10^{-6}$. Very roughly, this transition occurs around rotation periods of 3.5 days. There is some evidence that a low-activity plateau ($F_{\text{Si IV}}/F_{\text{bolom}} < 10^{-7}$) is reached around a rotation period of 20 days, but larger samples of slowly rotating stars are needed to fill out this trend. We fitted the Si IV activity-rotation

Table 3
Planet Host Flux Measurements

Name	F_{bol}^a (10^{-7} $\text{erg s}^{-1} \text{cm}^{-2}$)	N V (10^{-15} $\text{erg s}^{-1} \text{cm}^{-2} \text{\AA}^{-1}$)	C II (10^{-15} $\text{erg s}^{-1} \text{cm}^{-2} \text{\AA}^{-1}$)	Si III (10^{-15} $\text{erg s}^{-1} \text{cm}^{-2} \text{\AA}^{-1}$)	Si IV (10^{-15} $\text{erg s}^{-1} \text{cm}^{-2} \text{\AA}^{-1}$)	$F(90\text{--}360 \text{\AA})$ (10^{-14} $\text{erg s}^{-1} \text{cm}^{-2}$)
HD 120136	3.3	81.4 ± 0.9	...	164 ± 2	...	662
HD 197037	0.5	0.4 ± 0.1	4.1 ± 0.2	2.9 ± 0.1	2.7 ± 0.3	3.38
HD 136118	0.3	0.7 ± 0.1	6.5 ± 0.2	4.5 ± 0.2	3.9 ± 0.3	5.39
HD 9826	6.3	20 ± 1	132 ± 2	117 ± 4	45 ± 2	163
HD 10647	1.5	5.8 ± 0.2	46.2 ± 0.6	39.9 ± 0.6	29.0 ± 0.7	47.4
HD 23079	0.4	0.5 ± 0.1	3.4 ± 0.2	2.0 ± 0.2	2.6 ± 0.3	3.68
HD 155358	0.3	0.2 ± 0.1	1.7 ± 0.2	1.0 ± 0.1	0.8 ± 0.2	1.84
ρ CrB	1.8	1.2 ± 0.1	13.8 ± 0.3	7.2 ± 0.3	6.1 ± 0.3	9.43
HD 39091	4.6	2.4 ± 0.2	15.3 ± 0.3	8.8 ± 0.2	7.0 ± 0.3	19.7
HD 187085	0.3	0.5 ± 0.1	5.4 ± 0.2	3.4 ± 0.2	2.6 ± 0.2	4.40
HD 209458	0.2	0.7 ± 0.6	...	1.8 ± 0.3	...	5.74
HD 114729 A	0.5	0.5 ± 0.1	4.5 ± 0.2	2.7 ± 0.2	1.8 ± 0.2	4.35
HD 13931	0.2	0.7 ± 0.1	4.4 ± 0.2	2.4 ± 0.2	2.4 ± 0.3	5.76
47 UMa	2.7	3.4 ± 0.2	26.0 ± 0.5	14.2 ± 0.4	10.7 ± 0.4	27.7
HD 10180	0.3	0.7 ± 0.1	4.4 ± 0.2	2.4 ± 0.2	2.3 ± 0.2	5.58
HD 117618	0.3	0.5 ± 0.1	5.4 ± 0.2	2.6 ± 0.1	2.1 ± 0.2	4.19
HD 121504	0.2	1.1 ± 0.2	9.3 ± 0.3	6.7 ± 0.2	7.6 ± 0.3	9.02
μ Ara	1.9	3.6 ± 0.2	24.0 ± 0.4	13.2 ± 0.3	12.4 ± 0.4	29.2
16 Cyg B	0.7	...	13.5 ± 0.2	8.3 ± 0.1	7.4 ± 0.2	...
HD 1461	0.7	2.5 ± 0.1	13.6 ± 0.3	9.1 ± 0.2	8.7 ± 0.4	20.1
HD 38529	1.3	4.8 ± 0.2	24.9 ± 0.4	18.0 ± 0.4	14.9 ± 0.4	38.9
HD 37124	0.2	0.2 ± 0.1	5.0 ± 0.2	2.4 ± 0.2	2.8 ± 0.3	1.83
HD 147513	1.9	12.7 ± 0.6	0.4 ± 0.2	...	3.2 ± 0.6	103
HD 222582	0.2	0.4 ± 0.1	3.4 ± 0.2	1.9 ± 0.1	2.4 ± 0.3	3.44
HD 28185	0.2	0.7 ± 0.1	5.6 ± 0.2	2.1 ± 0.1	2.6 ± 0.3	5.54
HD 4113	0.2	0.6 ± 0.1	3.4 ± 0.2	1.7 ± 0.2	2.4 ± 0.3	4.62
HD 65216	0.3	0.6 ± 0.1	5.1 ± 0.3	3.1 ± 0.2	3.9 ± 0.3	5.06
HD 178911 B	0.2	1.1 ± 0.1	5.6 ± 0.2	3.8 ± 0.2	4.8 ± 0.4	8.70
HD 79498	0.2	0.4 ± 0.1	2.4 ± 0.2	1.8 ± 0.1	1.8 ± 0.3	3.50
HIP 91258	0.1	1.0 ± 0.3	3.7 ± 0.2	2.7 ± 0.2	4.1 ± 0.4	7.97
HD 90156	0.6	0.5 ± 0.1	5.7 ± 0.2	3.3 ± 0.2	3.1 ± 0.3	3.75
HD 115617	3.3	4 ± 2	28 ± 1	7 ± 3	12 ± 2	32.5
HD 70642	0.4	1.4 ± 0.1	8.5 ± 0.2	5.5 ± 0.2	5.5 ± 0.3	11.5
HD 47186	0.2	0.8 ± 0.1	3.9 ± 0.2	2.2 ± 0.2	3.1 ± 0.3	6.54
HD 92788	0.3	1.1 ± 0.1	7.4 ± 0.3	4.3 ± 0.2	4.1 ± 0.3	8.53
HD 102117	0.3	0.6 ± 0.1	3.8 ± 0.2	2.6 ± 0.2	2.5 ± 0.3	5.21
HD 4208	0.2	0.3 ± 0.1	2.6 ± 0.2	1.3 ± 0.1	1.5 ± 0.3	2.32
HD 10700	11.1	11.9 ± 0.7	66.0 ± 0.8	30 ± 2	16.9 ± 0.7	96.7
HD 69830	1.2	1.6 ± 0.1	14.8 ± 0.3	7.1 ± 0.2	8.0 ± 0.4	13.1
55 Cnc	1.2	3.04 ± 0.4	24.7 ± 0.1	15.9 ± 0.1	...	24.7
HD 1237	0.7	20.8 ± 0.7	0.2 ± 0.8	169
HD 154345	0.7	1.9 ± 0.1	14.8 ± 0.3	8.2 ± 0.2	7.3 ± 0.4	15.8
GJ 86	1.5	4.4 ± 0.2	36.2 ± 0.5	15.2 ± 0.6	15.4 ± 0.5	35.4
HD 147018	0.1	0.6 ± 0.1	4.2 ± 0.2	2.4 ± 0.2	3.8 ± 0.4	4.84
HD 164922	0.5	0.6 ± 0.1	6.4 ± 0.3	3.7 ± 0.2	3.9 ± 0.3	4.84
HD 189733	0.3	5.8 ± 0.1	31.6 ± 0.2	11.3 ± 0.1	12.4 ± 0.2	47.1
HD 7924	0.4	1.5 ± 0.1	10.1 ± 0.3	4.0 ± 0.2	5.7 ± 0.3	12.1
HD 3651	1.4	3.8 ± 0.2	33.6 ± 0.6	13.3 ± 0.3	16.5 ± 0.5	31.1
HD 128621	110.8	408 ± 2	2572 ± 3	1268 ± 4	1026 ± 2	3320
HD 114783	0.3	0.9 ± 0.1	7.7 ± 0.3	2.8 ± 0.2	3.3 ± 0.3	7.62
HD 97658	0.3	0.37 ± 0.04	2.45 ± 0.07	1.76 ± 0.06	1.42 ± 0.07	3.00
HD 40307	0.6	0.37 ± 0.04	2.76 ± 0.07	1.66 ± 0.06	1.47 ± 0.08	3.02
HD 192263	0.3	4.7 ± 0.2	25.7 ± 0.5	8.7 ± 0.2	10.6 ± 0.4	38.4
ϵ Eri	12.6	104 ± 1	451 ± 7	372 ± 2	335 ± 6	1200 ^b
HD 192310	1.7	4.9 ± 0.2	41.0 ± 0.7	14.5 ± 0.3	14.6 ± 0.5	39.4
HD 99492	0.4	1.8 ± 0.2	10.4 ± 0.3	3.6 ± 0.2	5.3 ± 0.4	15.0
HD 128311	0.3	8.5 ± 0.3	41.1 ± 0.6	14.0 ± 0.3	18.0 ± 0.5	68.8
HD 104067	0.3	3.0 ± 0.2	14.9 ± 0.4	5.1 ± 0.2	7.4 ± 0.4	24.5
HD 156668	0.1	0.4 ± 0.1	2.7 ± 0.2	1.1 ± 0.1	1.3 ± 0.3	3.00
HAT P 11	0.06	...	4.66 ± 0.09	1.17 ± 0.04
WASP 69	0.04	0.57 ± 0.02	2.59 ± 0.03	1.26 ± 0.2	...	4.64
HD 85512	0.5	0.69 ± 0.05	3.96 ± 0.08	1.72 ± 0.06	1.82 ± 0.09	5.59

Table 3
(Continued)

Name	$F_{\text{bol}}^{\text{a}}$ (10^{-7}) erg s $^{-1}$ cm $^{-2}$)	N V (10^{-15}) erg s $^{-1}$ cm $^{-2}$ Å $^{-1}$)	C II (10^{-15}) erg s $^{-1}$ cm $^{-2}$ Å $^{-1}$)	Si III (10^{-15}) erg s $^{-1}$ cm $^{-2}$ Å $^{-1}$)	Si IV (10^{-15}) erg s $^{-1}$ cm $^{-2}$ Å $^{-1}$)	$F(90\text{--}360 \text{ \AA})$ (10^{-14}) erg s $^{-1}$ cm $^{-2}$)
GJ 832	1.0	3.51 ± 0.08	3.78 ± 0.08	2.55 ± 0.06	3.33 ± 0.09	28.5
GJ 667 C	0.3	0.72 ± 0.05	0.65 ± 0.05	0.51 ± 0.04	0.83 ± 0.07	5.82
GJ 3470	0.02	3.0 ± 0.5	...	3.0 ± 0.9	...	24.4
GJ 176	0.09	3.10 ± 0.08	5.4 ± 0.1	2.15 ± 0.06	2.30 ± 0.09	25.2
GJ 436	0.08	0.96 ± 0.05	1.09 ± 0.06	0.52 ± 0.04	0.68 ± 0.07	7.77
GJ 1214	0.008	0.18 ± 0.04	0.09 ± 0.03	0.08 ± 0.03	0.05 ± 0.04	1.50
GJ 876	0.2	10.7 ± 0.1	10.6 ± 0.1	8.1 ± 0.1	8.4 ± 0.1	87.0
GJ 581	0.2	0.53 ± 0.04	0.48 ± 0.04	0.29 ± 0.04	0.44 ± 0.07	4.34
Proxima Centauri	0.29	38.7 ± 0.6	36.1 ± 0.4	12.6 ± 0.9	22.2 ± 0.5	150 ^b

Notes.^a $F_{\text{bol}} = \sigma T_{\text{eff}}^4 (R_*/d)^2$.^b Direct measurement of the 90–360 Å flux from *EUVE*, corrected for interstellar hydrogen and helium attenuation.

diagram with a power law of the form:

$$\log_{10} F_{\text{ion}}/F_{\text{bolom}} = \begin{cases} R_{\text{sat}}, & P_{\text{rot}} < P_{\text{break}} \\ R_{\text{sat}} \times (P_{\text{rot}}/P_{\text{break}})^{\alpha}, & P_{\text{rot}} \geq P_{\text{break}}. \end{cases} \quad (3)$$

where R_{sat} is the logarithmic saturated activity level and P_{break} is the turnover rotation period where the activity declines. We used the MCMC sampler *emcee* (Foreman-Mackey et al. 2013) to explore the posterior probability of the free parameters of this model (R_{sat} , P_{break} , α), modeling the data scatter as Gaussian in log space with constant standard deviation that we treated as a fourth free parameter. We applied a uniform prior of 1 day $< P_{\text{break}} < 10$ days based on the clear visual trend in the data and treated $P_{\text{rot}}/\sin i$ upper limits derived from $v \sin i$ measurements as equivalent to P_{rot} in the fits.

With sparse coverage of stars with rotation $P_{\text{rot}} < 3$ days, we are only able to place an upper limit on P_{break} for the ions studied here, $P_{\text{break}} \lesssim 3.5$ days. For all four ions, R_{sat} is between -5.5 and -6.0 . For the Si IV plot shown in Figure 4, $\alpha = -1.1 \pm 0.1$. For C II, $\alpha = -1.0 \pm 0.1$. For Si III, $\alpha = -1.1 \pm 0.1$. For N V, $\alpha = -1.3 \pm 0.1$.

The UV-activity rotation diagram is qualitatively reminiscent of the $H\alpha$ -rotation relationship for M dwarfs presented by Newton et al. (2017), as well as the X-ray-rotation relationship presented by Pizzolato et al. (2003) for cool stars. The transition to the low-activity UV state takes place at shorter rotation periods for cool stars as a whole, relative to M dwarf-only samples. This indicates that warmer stars “turn over” to a lower activity level at shorter rotation periods than for M stars. Due to the primary goals of the surveys that acquired our UV M dwarf observations, we have too few stars with intermediate rotation periods (10–30 days) to make a detailed comparison with the $H\alpha$ sample.

Figure 4 also indicates outliers on the high- and low-activity ends of the distribution: intermediate activity levels can be found out to rotation periods ≈ 100 days (Proxima Cen and GJ 876 due in some measure to flare activity during their UV observations; Christian et al. 2004; France et al. 2012; France 2016; Ribas et al. 2016), while anomalously low activity levels (HD 28033 and HD 13931) may be reminiscent of planet-induced rotational modulation, as has been suggested for WASP-18 (Pillitteri et al. 2014; Fossati et al. 2018).

4.1. Comparison with the Non-planet Host Control Sample

Figure 3 shows a clear bimodality of the UV activity index of our sample. The non-planet-hosting sample (open, black symbols) has activity levels roughly 5–10 times higher than that of the planet-hosting sample. At first glance, these plots suggest that non-planet-hosting stars are more active than their planet-hosting cousins, however, Figure 4 shows that this is clearly an effect of the different rotation periods sampled in the two populations. We can interpret the differences between the planet-hosting and non-planet-hosting samples as an age bias arising from the detection technique. The large RV surveys of the 1990s and 2000s made specific cuts on Ca II activity indices to avoid excess stellar jitter from higher activity stars making the extraction of the radial velocity signal more challenging (although see also Isaacson & Fischer 2010). Therefore, these surveys are biased by self-selection for ages $\gtrsim 2$ Gyr for solar-type stars (Marcy et al. 2004; Valenti & Fischer 2005); the exoplanet host star observations essentially give us a picture of the radiation environment at ages $\gtrsim 2$ Gyr. On the other hand, observations of the control sample were originally acquired in part because some of these systems were interesting active stars, and therefore provide a better picture of the typical UV irradiance level experienced by orbiting planets during the initial ~ 1.7 Gyr when life would be forming and evolving (Jones & Sleep 2010).

4.1.1. Individual “Like-star” Comparisons

A complementary approach to comparing the ensemble properties of planet-hosting and non-planet-hosting stars is to examine individual systems with very similar spectral types and rotation periods. The goal here is to find stars whose most obvious difference is the presence of a planetary system. We note that due to the limited size of the survey, finding systems with like-stellar parameters and like-planetary systems was not possible (e.g., HD 189733, ϵ Eri, and HD 128311 below). Using the Si IV activity index as representative of the behavior of the FUV emission from these stars, we identified the following “case studies” for comparison:

1. The $P_{\text{rot}} \sim 11$ day K dwarfs (see Tables 1 and 2 for stellar parameter references): comparing the similar planet-hosting stars HD 189733 (K0 V, $T_{\text{eff}} = 4880$ K, $P_{\text{rot}} = 13.4$ days), ϵ Eri (K2 V, $T_{\text{eff}} = 4900$ K, $P_{\text{rot}} = 11.7$ days), and HD

Table 4
Non-planet Host Flux Measurements

Name	$F_{\text{bol}}^{\text{a}}$ [10^{-7} erg s $^{-1}$ cm $^{-2}$]	N V [10^{-15} erg s $^{-1}$ cm $^{-2}$ Å $^{-1}$]	C II [10^{-15} erg s $^{-1}$ cm $^{-2}$ Å $^{-1}$]	Si III [10^{-15} erg s $^{-1}$ cm $^{-2}$ Å $^{-1}$]	Si IV [10^{-15} erg s $^{-1}$ cm $^{-2}$ Å $^{-1}$]	$F(90\text{--}360 \text{ \AA})$ [10^{-14} erg s $^{-1}$ cm $^{-2}$]
HD 28568	0.6	23 ± 5	120 ± 4	82 ± 8	65 ± 5	189
HD 28033	0.3	...	4.8 ± 0.9	1 ± 3	7 ± 2	...
HD 33262	2.8	47 ± 2	287 ± 2	319 ± 4	307 ± 3	380
HD 106516	1.2	4 ± 3	22 ± 2	4 ± 5	1 ± 4	32.6
HD 28205	0.3	8 ± 2	27 ± 2	22 ± 4	17 ± 3	67.8
HD 25825	0.2	10.6 ± 0.5	36.7 ± 0.7	40.9 ± 0.8	47 ± 1	86.2
HD 97334	0.7	15 ± 2	86 ± 2	48 ± 4	82 ± 2	121
HD 39587	4.3	...	454 ± 2	...	385 ± 2	680 ^b
HII 314	0.02	2.24 ± 0.08	6.8 ± 0.1	3.70 ± 0.9	4.8 ± 0.1	18.2
16 Cyg A	1.1	...	17.7 ± 0.2	10.8 ± 0.2	8.3 ± 0.2	...
HD 72905	1.5	...	184 ± 1	...	136 ± 1	...
HD 129333	0.3	...	124 ± 1	...	106 ± 1	...
HD 199288	0.6	0.31 ± 0.06	3.77 ± 0.07	1.79 ± 0.08	1.48 ± 0.09	2.53
α Cen A	271	356 ± 5	2690 ± 8	1590 ± 12	1220 ± 7	2900 ^b
HD 59967	0.6	18 ± 2	60 ± 2	71 ± 3	47 ± 2	145
HD 20630	3.3	39 ± 1	234 ± 2	216 ± 4	209 ± 2	40 ^b
HD 43162	0.7	3 ± 2	73 ± 2	48 ± 5	61 ± 3	22.8
HD 131156	3.9	70 ± 4	451 ± 6	281 ± 12	317 ± 5	830 ^b
KIC 11560431	0.0002	4.6 ± 1	16.4 ± 0.2	5.7 ± 0.1	6.9 ± 0.1	37.0
HD 166	1.1	43 ± 2	126 ± 3	96 ± 5	94 ± 3	350
HD 165341	6.9	71 ± 2	437 ± 2	249 ± 5	206 ± 2	700 ^b
HD 103095	1.9	0.1 ± 0.1	1.1 ± 0.1	0.56 ± 0.09	1.2 ± 0.1	1.11
HR 1925	1.3	21 ± 2	85 ± 2	63 ± 4	56 ± 2	171
HD 22468	2.6	600 ± 3	2550 ± 5	1280 ± 12	1200 ± 4	4880
HD 155886	2.6	19 ± 1	131 ± 1	66 ± 2	...	151
LTT 2050	0.06	1.7 ± 0.1	2.0 ± 0.2	0.58 ± 0.09	1.4 ± 0.2	13.6
HD 197481	0.2	70 ± 1	206 ± 2	788 ± 2	864 ± 1	720 ^b
Kapteyn's Star	0.3	0.2 ± 0.1	0.9 ± 0.1	0.8 ± 0.1	0.9 ± 0.3	1.98
LP 415-1619	0.006	...	2.97 ± 0.07	0.77 ± 0.04
AD Leo	0.2	136 ± 1	219 ± 1	142 ± 1	159 ± 1	1100 ^b
LHS-26	0.08
Procyon	170	1650 ± 5	8720 ± 9	4940 ± 10	4160 ± 20	3500 ^b
EV Lac	0.2	41 ± 1	51 ± 10	35 ± 2	39 ± 1	450 ^b
YY Gem	0.1	41.7 ± 0.7	223 ± 1	34 ± 1	82 ± 1	339

Notes.

^a $F_{\text{bol}} = \sigma T_{\text{eff}}^4 (R_*/d)^2$.

^b Direct measurement of the 90–360 Å flux from *EUVE*, corrected for interstellar H I attenuation.

128311 (K3 V, $T_{\text{eff}} = 4965$ K, $P_{\text{rot}} = 14$ days) with the non-planet-hosting K dwarf HR 1925 (K1 V, $T_{\text{eff}} = 5309$ K, $P_{\text{rot}} = 10.86$ days), we find the average $F_{\text{Si IV}}/F_{\text{bolom}}$ value for the planet-hosting stars is $4.3 (\pm 0.2) \times 10^{-7}$, while HR 1925 displays the identical $4.3 (\pm 0.2) \times 10^{-7}$.

2. The $P_{\text{rot}} \sim 28$ day G dwarfs: comparing the similar planet-hosting stars μ Ara (G3 V, $T_{\text{eff}} = 5800$ K, $P_{\text{rot}} = 31$ days), 16 Cyg B (G3 V, $T_{\text{eff}} = 5770$ K, $P_{\text{rot}} = 29.1$ days), and HD 1461 (G3 V, $T_{\text{eff}} = 5765$ K, $P_{\text{rot}} = 29$ days) with the non-planet-hosting G dwarfs 16 Cyg A (G1.5 V, $T_{\text{eff}} = 5825$ K, $P_{\text{rot}} = 26.9$ days) and α Cen A (G2 V, $T_{\text{eff}} = 5770$ K, $P_{\text{rot}} = 29$ days), we find the average $F_{\text{Si IV}}/F_{\text{bolom}}$ value for the planet-hosting stars is $9.8 (\pm 0.6) \times 10^{-8}$, while the non-planet-hosting sample displays the somewhat lower $6.0 (\pm 0.2) \times 10^{-8}$.

3. The $P_{\text{rot}} \sim 100$ day M dwarfs: comparing the planet-hosting star GJ 667C (M1.5 V, $T_{\text{eff}} = 3440$ K, $P_{\text{rot}} = 105$ days) with the non-planet-hosting Kapteyn's Star (M1 V, $T_{\text{eff}} = 3527$ K, $P_{\text{rot}} = 84.7$ days), we see that $F_{\text{Si IV}}/F_{\text{bolom}}$ for GJ 667C is $2.7 (\pm 0.2) \times 10^{-8}$, while

Kapteyn's star displays a statistically indistinguishable $3.0 (\pm 1.0) \times 10^{-8}$.

The comparisons above show that other than a slightly higher Si IV activity level in the solar-type planet-hosting stars, there is essentially no discernible difference between the FUV activity levels of the planet-hosting and non-planet-hosting samples. This supports the assertion made above that we are observing an age spread of a single stellar population as opposed to two distinct planet-hosting and non-planet-hosting groups.

4.1.2. FUV Activity Index as a Proxy for EUV Irradiance

The stellar EUV energy budget contains contributions from both the transition region (Lyman continuum as well as helium and metal line emission in the 228–911 Å bandpass) and corona. The FUV emission lines (N V and Si IV) are required to estimate the former (Fontenla et al. 2011; Linsky et al. 2014), while X-ray data provide constraints on the latter (e.g., Sanz-Forcada et al. 2011).

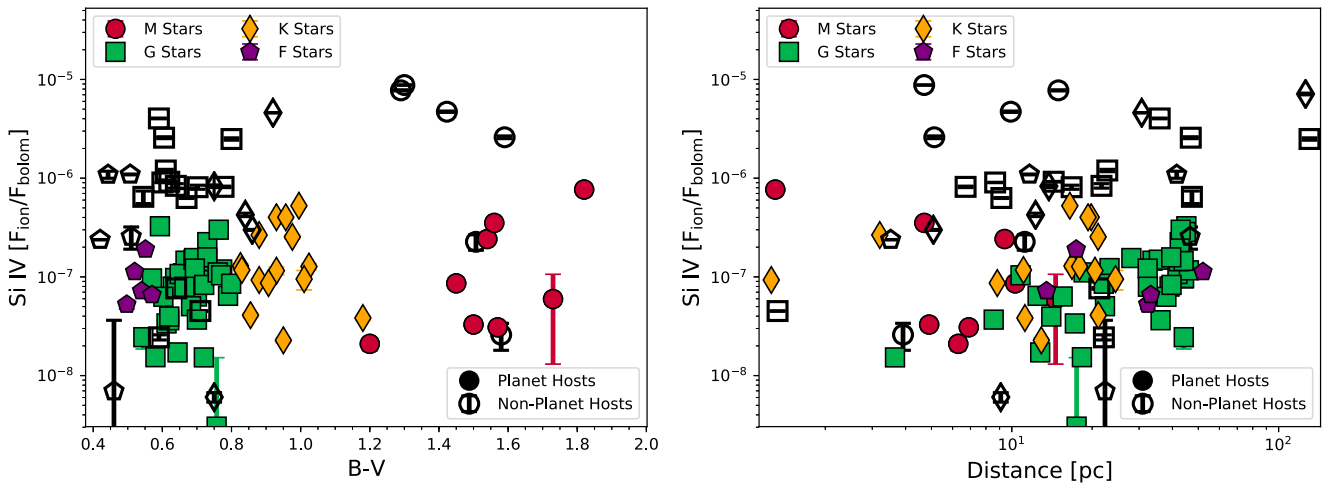


Figure 3. The full planet-hosting sample (in filled color symbols) and non-planet control sample (in open black symbols), showing Si IV fractional hot gas luminosity as a function of $B - V$ color (left, a proxy for effective surface temperature) and distance (right). Spectral types are given by different symbols (circles: M dwarfs; diamonds: K dwarfs; squares: G dwarfs; pentagons: F dwarfs) as shown in the legend. The non-planet-hosting stars are shown to be systematically factors of 5–10 brighter in the high-temperature FUV lines. The Si IV behavior is representative of the behavior of all 4 FUV activity indicators studied here; the full plot set is presented in Appendix B.

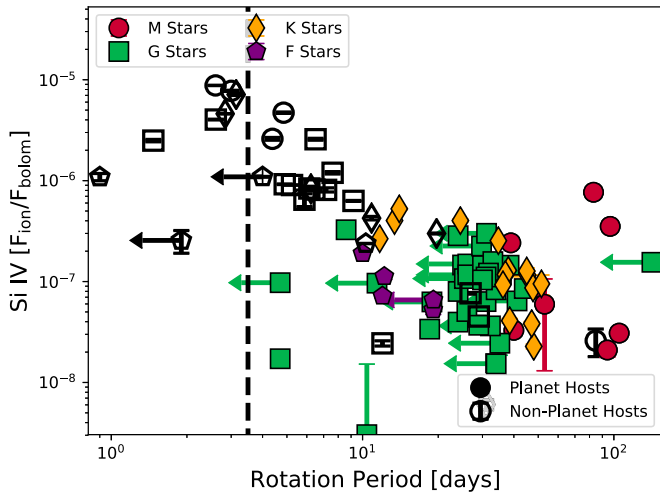


Figure 4. The full planet-hosting sample (in filled color symbols) and non-planet control sample (in open black symbols), showing the Si IV activity level (\propto fractional hot gas luminosity) as a function of the stellar rotation period (P_{rot}). Spectral types are given by different symbols (circles: M dwarfs; diamonds: K dwarfs; squares: G dwarfs; pentagons: F dwarfs) as shown in the legend. This figure succinctly demonstrates the bimodal distribution of targets, with non-planet hosts typically having $P_{\text{rot}} \lesssim 20$ days and the planet hosts having $P_{\text{rot}} \gtrsim 20$ days. This is a natural consequence of the selection bias for RV planet searches (Marcy et al. 2004). The saturated activity level is $\log_{10} F_{\text{Si IV}}/F_{\text{bolom}} \approx -5.6$, and the power-law slope beyond the $P_{\text{orb}} \approx 3.5$ day break point is -1.1 ± 0.1 (Section 4.1).

We combine our large FUV data set with the smaller number of overlapping *EUVE* observations to: (1) evaluate if the UV transition region emission lines directly scale with the EUV flux and if so (2) present a new method for estimating the 90–360 Å flux from cool stars. Both of these topics are critical to modeling the atmospheric response of all types of planets, from rocky worlds (Lammer et al. 2009; Wheatley et al. 2017) to hot Jupiters (Murray-Clay et al. 2009; Koskinen et al. 2013).

We find that the FUV activity indices that we presented in Section 3 can be correlated with the comparable EUV fractional luminosity to develop scaling relations for the EUV flux that hold across spectral type and activity level. These relations do not rely on Ly α flux reconstructions or scalings

from other lines to estimate the Ly α flux.⁷ Other than local ISM absorption of the ground-state C II 1334 Å line, our FUV activity measurements are straightforward and do not suffer from any significant line-of-sight attenuation or uncertain intrinsic emission line shapes (see, e.g., the discussion of the intrinsic Ly α emission line profiles of cool stars in Wood et al. 2005 and Youngblood et al. 2016). We parameterize the 90–360 Å flux as a function of the UV activity indices presented above:

$$\log_{10}(F(90 - 360 \text{ \AA})/F_{\text{bolom}}) = m \times \log_{10}(F_{\text{ion}}/F_{\text{bolom}}) + b, \quad (4)$$

(see Figure 5), where the wavelength range (90–360) is in Å. We computed the residuals for each ion (defined as the difference between the $F(90-360 \text{ \AA})/F_{\text{bolom}}$ data and the best-fit linear model), and unsurprisingly, the FUV lines with the highest formation temperature showed the smallest residuals. We therefore favor NV and Si IV as the best proxies for the fractional EUV flux. The rms scatter on the residuals for these two ions are between factors of 1.7 and 1.8 in linear flux, even though both flux ratios span approximately two and half orders of magnitude in activity level. The best-fit coefficients for the UV activity index-to-EUV activity for NV are $[m, b] = [1.0 (\pm 0.1), 1.9 (\pm 0.6)]$, and the coefficients for Si IV are $[m, b] = [1.3 (\pm 0.1), 3.5 (\pm 0.8)]$.⁸

While we recommend transition region tracers (Si IV and NV) because these lines are formed in plasma conditions closer to the EUV emission and do not suffer from ISM absorption effects, a correlation exists with the lower-temperature chromospheric lines as well (C II). The best-fit coefficients for the UV activity index-to-EUV activity for C II are $[m, b] = [1.4 (\pm 0.2), 3.5 (\pm 0.9)]$. The C II–EUV correlation

⁷ Ly α flux reconstructions and Ly α scaling relations have uncertainties that can range from 20% to factors-of-several depending on the signal-to-noise and spectral resolution of the observations (Linsky et al. 2014).

⁸ We note that Proxima Cen is the only star in this sample with a planet inside 0.2 au. Excluding Proxima from the fits does not change the fit coefficients beyond their 1σ uncertainty ranges.

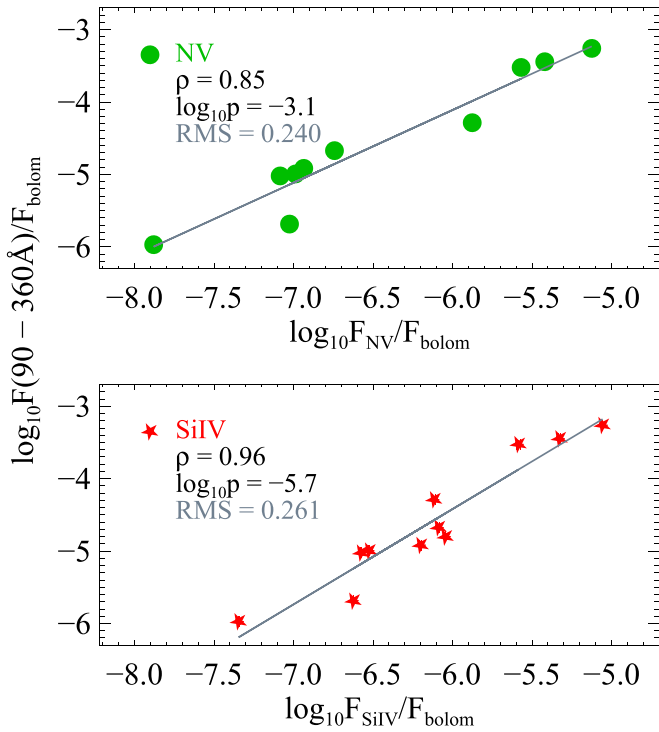


Figure 5. Correlations between the N V (top) and Si IV (bottom) activity index and the fractional 90–360 Å flux (from archival *EUVE* observations). The *EUVE* fluxes have been corrected for interstellar H I opacity. The Spearman rank coefficient (ρ), the p -value, and the rms scatter about the best-fit line are shown in the legend. The tight correlation argues that broadband EUV fluxes in this region can be estimated to within a factor of ~ 2 from the FUV activity index.

has larger scatter than those for Si IV and N V; the higher ionization relationships should be used when possible.

Based on the above analysis, we determine that (1) the EUV fluxes follow a power-law relationship with the FUV transition region activity indices over a wide range of spectral types and rotation periods and (2) with an estimate of the star’s bolometric luminosity and a measurement of one of the higher temperature FUV emission lines, the stellar EUV flux in the 90–360 Å band can be estimated to roughly a factor of two. Using the above relationship for N V, we calculated the 90–360 Å flux for all stars in the survey and these are presented in Tables 3 and 4. The computed EUV fluxes are plotted as a function of stellar rotation period in Figure 6. The largest uncertainties on calculated $F(90\text{--}360\text{ Å})$ come from the uncertainties on the linear fit parameters, which correspond to approximately a factor of 2.3 uncertainty on $F(90\text{--}360\text{ Å})$ when using the N V–EUV relations.

A rough estimate of the total EUV irradiance can be computed for the quiet Sun (Woods et al. 2009) and an inactive M dwarf (GJ 832) using the model spectra of Fontenla et al. (2016). $F_{\star}(90\text{--}911\text{ Å}) = F(90\text{--}360\text{ Å}) + F(360\text{--}911\text{ Å})$. For the quiet Sun,

$$F_{G2V}(90\text{--}911\text{ Å}) = F(90\text{--}360\text{ Å}) + [0.57 \times F(90\text{--}360\text{ Å})]. \quad (5)$$

For a quiescent M1V star,

$$F_{M1V}(90\text{--}911\text{ Å}) = F(90\text{--}360\text{ Å}) + [1.12 \times F(90\text{--}360\text{ Å})], \quad (6)$$

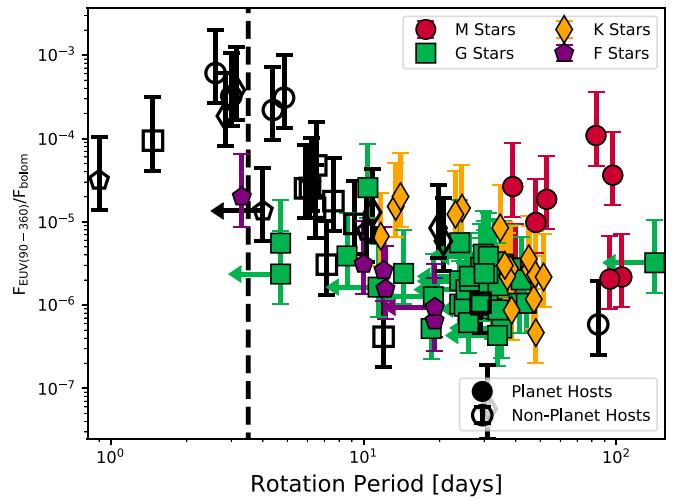


Figure 6. Converting the N V UV activity index to the relative EUV flux in the 90–360 Å band (Equation (4)), we calculate the ISM-corrected $F(90\text{--}360\text{ Å})/F_{\text{bolom}}$ flux ratio for all stars in our sample with N V measurements. EUV error estimates are propagated from the uncertainty on the best-fit parameters to Equation (4). One observes a \sim two-order-of-magnitude decline in the EUV emission strength as cool stars move from the saturated activity regime at rotation periods $P_{\text{rot}} \lesssim 3.5$ days to the presumably older population at $P_{\text{rot}} \gtrsim 20$ days.

where $F(90\text{--}360\text{ Å})$ is the computed EUV flux described above. We note that because the Si IV and N V formation temperatures are an order of magnitude (or more) less than the typical coronal temperature of these stars, we do not suggest extending these relations to the X-ray wavelengths (5–100 Å). We refer the reader to Poppenhaeger et al. (2010), Sanz-Forcada et al. (2011), and Loyd et al. (2016) for a discussion about the X-ray properties of planet-hosting stars of various spectral types.

These results argue that the EUV evolution from younger to older stars (shorter to longer rotation periods) is similar to that from the chromospheric/transition region emission. X-ray +EUV evolution studies for solar-type stars (Ribas et al. 2005) find a comparable decrease ($\sim 10\text{--}20$ in the 20–360 Å band) for solar type stars from ~ 0.6 Gyr to ~ 4 Gyr. The two results suggest a common picture where the overall XUV + FUV (5–1800 Å) flux decreases by one to two orders of magnitude as the stars age from ~ 0.5 to 5 Gyr. This result is consistent with the relative FUV flux decline in the *GALEX* sample of early M dwarfs presented by Schneider & Shkolnik (2018).

What are the potential impacts of this flux evolution on orbiting planets? For terrestrial atmospheres, increasing the EUV flux to levels estimated for the young Sun (~ 1 Gyr; Ayres 1997) can increase the temperature of the thermosphere by a factor of $\gtrsim 10$ (Tian et al. 2008), potentially causing significant and rapid atmospheric mass-loss. The issue of increased EUV irradiance and the atmospheric stability of rocky planets (see, e.g., Lammer et al. 2018) is even greater for M dwarfs, where the EUV irradiance levels of even field-age stars (ages $\sim 2\text{--}6$ Gyr) are predicted to drive runaway oxidation as many Earth oceans worth of hydrogen are lost (e.g., Ribas et al. 2016; Wheatley et al. 2017). Our results provide an estimate of the enhancement level of the total EUV + FUV radiation environment around F through M stars, anchored by direct observations.

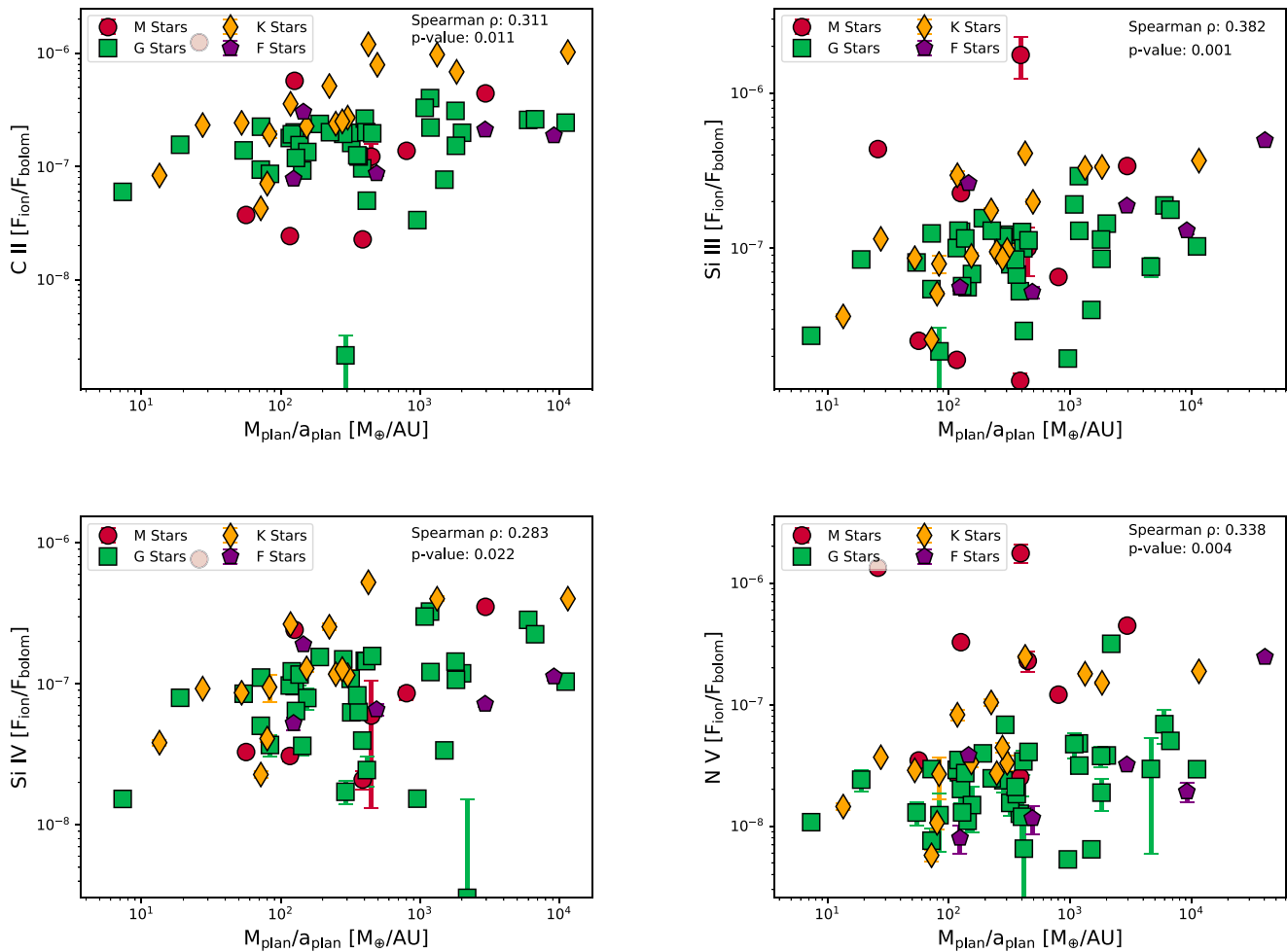


Figure 7. UV activity levels as a function of the “SPI parameter” ($M_{\text{plan}}/a_{\text{plan}}$) for (top left to lower right) Si III λ 1206 Å, N V λ 1240 Å, C II λ 1335 Å, and Si IV λ 1400 Å. Spectral types are given by different symbols (circles: M dwarfs; diamonds: K dwarfs; squares: G dwarfs; pentagons: F dwarfs) as shown in the legend. All UV activity vs. SPI parameter correlations have Spearman rank coefficients between 0.28 and 0.38, with p -values between 1×10^{-3} and 2×10^{-2} . While the UV activity vs. SPI parameter correlations are all statically significant, underlying correlations with the stellar parameters driven by population selection biases are also present (see Section 4.2.2). Section 4.2 describes the analysis of alternative SPI proportionalities.

4.2. UV Activity Diagnostics and SPIs

Figure 7 shows the UV activity indices versus the SPI parameter ($M_{\text{planet}}/a_{\text{planet}}$), assuming the mass and semimajor axis of the most massive planet in multi-planet systems, for the sample of planet-hosting stars. The results are quantitatively similar when calculating the correlations with the closest planet. We find a significant linear correlation between the fractional luminosities for all four ions and the SPI parameter, suggesting that stars with more massive and close-in planets emit more ultraviolet photons from their chromospheres and transition regions relative to their bolometric luminosity. In Figure 7, Spearman ρ and p -values are calculated for the \log_{10} SPI versus $\log_{10} F_{\text{ion}}/F_{\text{bolom}}$ relations.⁹ We find that for N V, $[\rho_{\text{N V}}, p_{\text{N V}}] = [0.303, 0.016]$, for C II, $[\rho_{\text{C II}}, p_{\text{C II}}] = [0.296, 0.019]$, for Si III, $[\rho_{\text{Si III}}, p_{\text{Si III}}] = [0.343, 0.005]$, and for Si IV, $[\rho_{\text{Si IV}}, p_{\text{Si IV}}] = [0.315, 0.015]$. In addition to the p -values all being at statistically significant levels, Spearman

⁹ The p -value is a measure of the ability of the distribution to be consistent with a null correlation, i.e., an uncorrelated scatter plot. A p -value of 1 is a perfect scatter plot and p -values of less than 0.05 typically indicate a strong correlation for sample sizes larger than a few tens of data points.

coefficients near 0.3 for samples sizes between 60 and 80 (our sample has 71 stars) represent a statistically significant correlation at the $\sim 99\%$ confidence level.

This result confirms the general trend between \log_{10} SPI versus $\log_{10} F_{\text{ion}}/F_{\text{bolom}}$ identified for M dwarfs by France et al. (2016a), with the caveat that our larger sample identifies significant stellar and observational biases that may drive this result (see Section 4.2.1). Our spectroscopic line sample does not include lower-formation-temperature species like Si II and Mg II, so we are unable to test the fall-off of this correlation with atmospheric emitting region temperature. We confirm that over the roughly 20,000–200,000 K temperature range spanned by our four target ions, this trend holds. Care should be taken in parsing this sample up into sub-categories, as individual flare events, stellar activity cycles, or specific star–planet systems will more strongly influence the results. With that caveat in mind, we note that the correlation coefficients of the full sample are quite a bit lower than those found by France et al. for the MUSCLES stars ($\rho \gtrsim 0.6$). The \log_{10} SPI versus $\log_{10} F_{\text{ion}}/F_{\text{bolom}}$ correlations are much stronger in our (albeit small) sample of K dwarfs compared to the full F – M sample. The Spearman ρ coefficients and p -values for the K dwarf

Table 5
Correlations between SPI Parameters and $F_{\text{ion}}/F_{\text{bolom}}$

ion	SPI Parameter	ρ	p -value	ΔBIC	Improved BIC
N V	$M_{\text{plan}}/a_{\text{plan}}$	0.338	0.004	0.0172	with SPI
Si III	$M_{\text{plan}}/a_{\text{plan}}$	0.382	0.001
Si IV	$M_{\text{plan}}/a_{\text{plan}}$	0.283	0.022
C II	$M_{\text{plan}}/a_{\text{plan}}$	0.311	0.011
N V	$M_{\text{plan}}^{2/3} (a_{\text{plan}}/R_*)^{-4} a_{\text{plan}}^{-1/2}$	0.300	0.017	4.089 ^a	without SPI
Si III	$M_{\text{plan}}^{2/3} (a_{\text{plan}}/R_*)^{-4} a_{\text{plan}}^{-1/2}$	0.108	0.392
Si IV	$M_{\text{plan}}^{2/3} (a_{\text{plan}}/R_*)^{-4} a_{\text{plan}}^{-1/2}$	0.047	0.725
C II	$M_{\text{plan}}^{2/3} (a_{\text{plan}}/R_*)^{-4} a_{\text{plan}}^{-1/2}$	0.087	0.503
N V	$M_{\text{plan}}^2 a_{\text{plan}}^{-1/2}$	0.053	0.679	4.056 ^a	without SPI
Si III	$M_{\text{plan}}^2 a_{\text{plan}}^{-1/2}$	0.264	0.034
Si IV	$M_{\text{plan}}^2 a_{\text{plan}}^{-1/2}$	0.277	0.034
C II	$M_{\text{plan}}^2 a_{\text{plan}}^{-1/2}$	0.210	0.101
N V	$(M_{\text{plan}}/M_*)^2 (a_{\text{plan}}/R_*)^{-6}$	0.319	0.011	4.081 ^a	without SPI
Si III	$(M_{\text{plan}}/M_*)^2 (a_{\text{plan}}/R_*)^{-6}$	0.146	0.246
Si IV	$(M_{\text{plan}}/M_*)^2 (a_{\text{plan}}/R_*)^{-6}$	0.089	0.505
C II	$(M_{\text{plan}}/M_*)^2 (a_{\text{plan}}/R_*)^{-6}$	0.115	0.376

Notes. ρ is the Spearman rank coefficient, where $|\rho| = 1$ for a perfect correlation and $\rho = 0$ when the data are uncorrelated. The p -value indicates the likelihood of obtaining $|\rho|$ closer to 1, under the assumption that there is no correlation between the two parameters (i.e., the data are randomly distributed).

^a The larger ΔBIC values in the latter three SPI parameters are the result of four PCs being required to fit the $F_{\text{ion}}/F_{\text{bolom}}$ distribution as opposed to the three PCs for the SPI parameter set to $M_{\text{plan}}/a_{\text{plan}}$ (see Section 4.2 and Appendix C).

sample are between 0.77–0.79 and $p < 0.002$, respectively, for all four ions.

We also considered other potential proportionalities between the UV power deposition and the star–planet system architecture that may provide clues about the physical mechanism responsible for enhanced atmospheric heating. Specifically, we explored (1) magnetic reconnection between stellar and planetary magnetic fields (Lanza 2012), with $F_{\text{ion}}/F_{\text{bolom}} \propto M_{\text{plan}}^{2/3} (a_{\text{plan}}/R_*)^{-4} a_{\text{plan}}^{-1/2}$, (2) magnetic loop stresses between the stellar and planetary fields (Lanza 2013), $F_{\text{ion}}/F_{\text{bolom}} \propto M_{\text{plan}}^2 a_{\text{plan}}^{-1/2}$, and (3) tidal torques (e.g., Zahn 2008), with $F_{\text{ion}}/F_{\text{bolom}} \propto (M_{\text{plan}}/M_*)^2 (a_{\text{plan}}/R_*)^{-6}$. Unlike the case of the “simple” SPI parameter, $M_{\text{plan}}/a_{\text{plan}}$, we did not find strong and consistent evidence for correlations between any of these alternative SPI metrics and the fractional UV. The N V–SPI correlation was significant for both the magnetic reconnection and tidal torque scenario, but this did not hold across the other ions. Table 5 presents the Spearman rank coefficients and p -values for each of these cases.

4.2.1. Underlying Stellar Correlations and Planet-hosting Sample Bias

Although there appears to be a significant power-law relationship between the SPI parameter and the fractional luminosities in N V, C II, Si III, and Si IV, it is possible that the trend is produced by observational biases within the sample of planet hosts. Stellar sample biases will serve to limit the detectable bounds of the SPI that can be confidently claimed. To investigate this effect, Spearman rank coefficients were calculated between the SPI parameter and stellar rotation period (P_{rot}), effective temperature (T_{eff}), distance (d), V , and $B - V$ (see Table 6). We find that the SPI parameter is correlated with P_{rot} ($\rho = -0.371$) and d ($\rho = 0.351$), at the same level as the SPI parameter is correlated with the UV activity indices.

The underlying dependencies on the stellar parameters can be understood by considering stellar and observational biases toward detecting certain types of planets. First, we find an inverse correlation between the SPI parameter and the rotation period (Figure 8, right). The RV detection method is less sensitive to lower-mass planets around more active stars because the stellar activity adds noise to the RV signal, therefore, only the most massive short-period planets are found around stars with small rotation periods. Second, we see a correlation of SPI with distance, which we also attribute to an observational bias: for fainter stars, only large RV signals are able to be clearly detected above the photon shot noise. Given a sample with similar stellar properties (e.g., K and G dwarfs), RV searches will only be sensitive to massive short period planets as the stars become fainter, that is, only planets with large $M_{\text{plan}}/a_{\text{plan}}$ will be readily detected at large distances. This finding is similar to conclusions from previous X-ray SPI analyses demonstrating that the correlation between planet mass and X-ray luminosity was driven by distance effects and stellar sample biases (Poppenhaeger & Schmitt 2011).

Because of the interdependency of the stellar parameters, an increase in the value of the SPI parameter cannot be directly associated with an enhancement in fractional luminosity. However, the impact of the SPI parameter can still be investigated by properly accounting for the stellar properties in our analysis, as discussed in the following subsection.

4.2.2. Statistical Analysis of SPI Signal

One method of incorporating the stellar parameters is to assume that each, like the SPI parameter, contributes linearly to the UV activity index. In a multiple linear regression model, a coefficient β represents the amount added by the corresponding parameter. However, the stellar properties themselves are correlated (e.g., $B - V \propto T_{\text{eff}}$; see Table 6), which complicates

Table 6
Correlations between Stellar Parameters: Planet Hosts

	P_{rot}		T_{eff}		d		V		$B - V$		$\log(SPI)$	
	ρ	p -value	ρ	p -value	ρ	p -value	ρ	p -value	ρ	p -value	ρ	p -value
P_{rot}	-0.612	1×10^{-8}	-0.338	1×10^{-3}	0.298	1×10^{-2}	0.648	1×10^{-9}	-0.371	1×10^{-3}
T_{eff}	-0.612	1×10^{-8}	0.506	6×10^{-6}	-0.475	2×10^{-5}	-0.931	3×10^{-32}	0.174	0.1
d	-0.338	1×10^{-3}	0.506	6×10^{-6}	0.305	9×10^{-3}	-0.473	3×10^{-5}	0.351	3×10^{-3}
V	0.298	0.01	-0.475	2×10^{-5}	0.305	9×10^{-3}	0.481	2×10^{-5}	0.191	0.1
$B - V$	0.648	1×10^{-9}	-0.931	3×10^{-32}	-0.473	3×10^{-5}	0.481	2×10^{-5}	-0.194	0.1
$\log(SPI)$	-0.371	1×10^{-3}	0.174	0.1	0.351	3×10^{-3}	0.191	0.1	-0.194	0.1

Note. ρ is the Spearman rank coefficient, where $|\rho| = 1$ for a perfect correlation and $\rho = 0$ when the data are uncorrelated. The p -value indicates the likelihood of obtaining $|\rho|$ closer to 1, under the assumption that there is no correlation between the two parameters (i.e., the data are randomly distributed). Here, we define “significant” correlations here as having $|\rho| > 0.3$ (marked in bold for the correlations with SPI); see Section 4.2.

the standard interpretation. To remove this bias, we first conduct a principal component analysis (PCA) to map the stellar properties and the SPI parameter into a new basis.

The purpose of the PCA is to transform the multiple linear regression model into a domain where the “predictor variables,” or principal components (PCs), are independent and orthogonal to each other (Pearson 1901). Each PC is constructed as a linear combination of the original variables, which in our case are the stellar parameters and the SPI parameter. A full description is presented in Appendix C. We reduce the problem to a set of three PCs, with PC₁ being most strongly correlated with P_{rot} , $B - V$, distance, and T_{eff} . The SPI parameter contributes more strongly to PC₂ and PC₃.

Equations (9) and (11) list the coefficients (β) of the multiple linear regression analysis in the PCs. The results show that three of the PCs contribute significantly to the observed linear relationship with the N V fractional luminosities (Figure 9, left). However, only PC₂ and PC₃ add to the Si III and Si IV fractional luminosities, and C II is only significantly dependent on PC₃. When we calculate the Spearman rank coefficients between the multiple linear regression models and fractional luminosities for each ion we find that the correlations appear to decrease with formation temperature. N V, with the highest formation temperature, has $\rho = 0.58$, while C II, with the lowest formation temperature, has $\rho = 0.33$. Si III and Si IV fall closer to C II, with $\rho = 0.32$ and $\rho = 0.33$ for both Si III and Si IV, respectively.

While these Spearman coefficients suggest a stronger correlation with the highest ionization emission line, one needs to evaluate the statistical significance of the importance of the SPI parameter to the observed UV activity levels. We do this by computing the Bayesian Information Criterion (BIC; Schwarz 1978) in the $F_{\text{N V}}/F_{\text{bolom}}$ versus linear regression plots with and without the SPI term. We find that the BIC does not change appreciably with the inclusion of the SPI term in the PCs of the linear regression. Figure 9 (right) shows the same PCA analysis for N V with the SPI information excluded from the regression models. We conclude that the SPI does not play an explicit role in shaping the distribution of UV activity indices in our sample. Appendix C.1 describes a comparable analysis of the non-planet-hosting stars.

Do these results mean that SPIs are not enhancing the FUV activity indices? Not necessarily. Models of both magnetic and tidal SPI indicate that one influence of the planet would be to spin-up the host star, disrupting nominal gyrochronological relationships (Lanza 2010; Brown 2014; Maxted et al. 2015). Indeed, we observe a correlation between the SPI parameter and the stellar rotation period (Figure 8, right). This may indicate that what we

observe as a “stellar interdependence” may in fact be a planet-induced effect whereby the interaction with the planetary system is altering the underlying stellar population. However, if we assume that the rotation period is strongly correlated with the UV activity level, an open question is why the exoplanet host stars as a group are not spun-up to the level of the non-planet-hosting sample.

5. Summary

We have presented a survey of UV emission line activity indices in F, G, K, and M dwarf exoplanet host stars. We analyzed the largest FUV spectroscopic data set of planet-hosting stars (71) assembled to date. This was complemented by a control sample of 33 stars not currently known to host planets. These observations were taken from a combination of archival and new programs with *HST*-COS and -STIS, targeting the chromospheric and transition region emission lines of Si III λ 1206 Å; $\log_{10} T_{\text{form}} = 4.7$, N V λ 1240 Å; $\log_{10} T_{\text{form}} = 5.2$, C II λ 1335 Å; $\log_{10} T_{\text{form}} = 4.5$, and Si IV λ 1400 Å; $\log_{10} T_{\text{form}} = 4.9$. We studied this data set to compare the UV activity properties of planet-hosting and non-planet-hosting systems, assess the connection between the FUV and EUV irradiance levels incident on orbiting planets, and to search for enhanced stellar activity that may result from the interaction of the planet and the host star.

The main results of this work are as follows:

1. The planet-hosting and non-planet-hosting samples display a bimodal distribution in FUV activity level, with the planet-hosting stars factors of 5–10 *fainter* in high-energy emission lines than the non-planet hosts. This can be explained by a sample bias: exoplanet host stars bright enough to obtain UV observations largely come from radial-velocity surveys that specifically select for low-activity stars. Conversely, previous observations of stars in the solar neighborhood often were originally targeted specifically because of their high levels of activity. Thus, we are largely seeing the difference between a field population of young (shorter rotation period) non-planet-hosting stars and an older (longer rotation period) exoplanet host star population. While this result is straightforward, it does present a note of caution for researchers modeling exoplanetary atmospheres: by selecting stellar irradiance levels based solely on samples of exoplanet host stars, one is underestimating the flux levels seen earlier in that planet’s evolution by an order of magnitude or more.
2. We have compared the FUV activity indices measured in this work with a sample of overlapping stars with

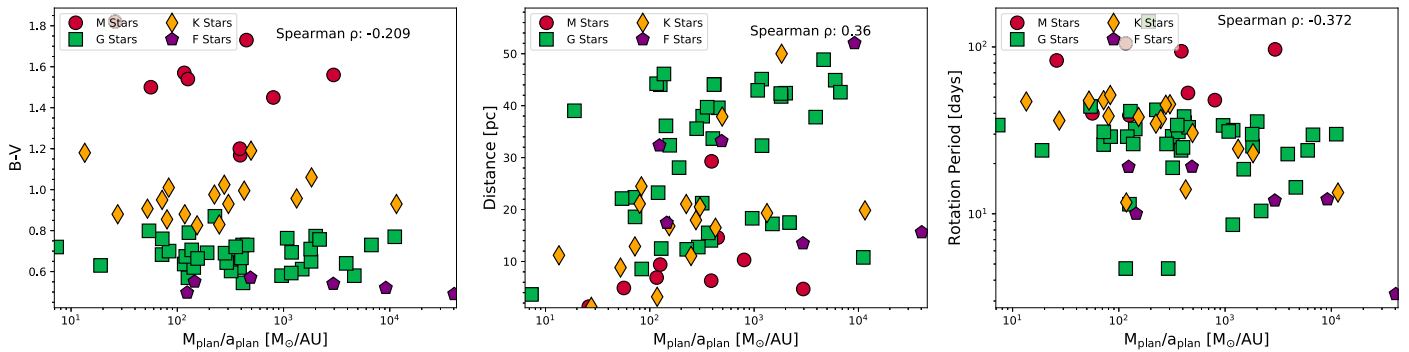


Figure 8. We investigate underlying stellar correlations by comparing $B - V$ (left), distance (center), and P_{rot} (right) vs. the SPI parameter. All plotting symbols are the same as Figure 7 (and shown in the legend) and the Spearman ρ coefficients are listed in the upper right corner of each figure.

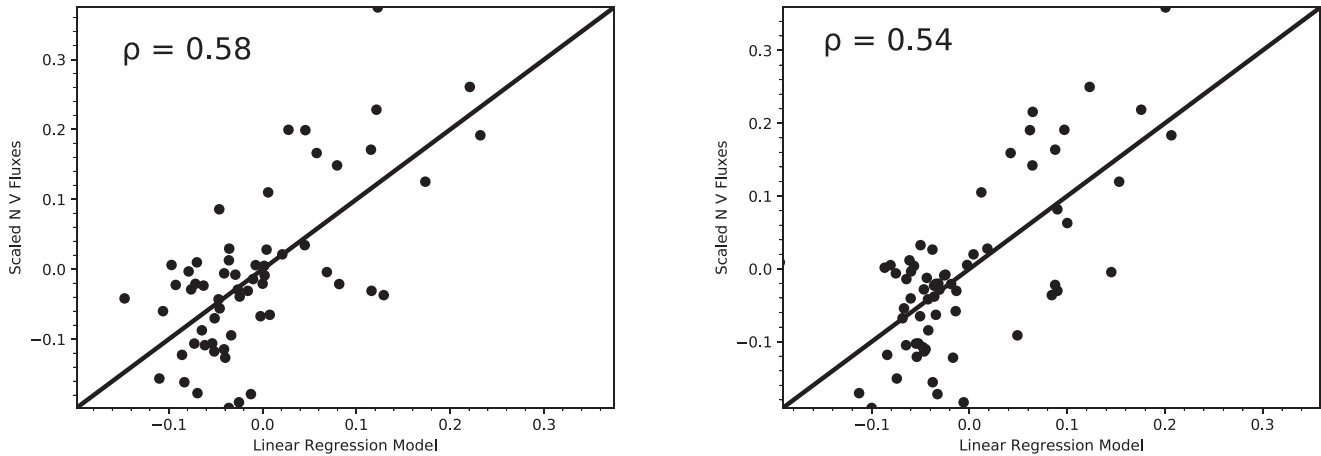


Figure 9. (Left) Comparison of the observed N V fluxes vs. those fluxes predicted from a PCA analysis incorporating stellar and planetary properties. (Right) The same PCA analysis without the SPI parameter included; the two analyses do not show statistically significant differences (Section 4.2.2). The Spearman correlation coefficient ρ describes the agreement between the multivariate linear model and our observations, where we expect $|\rho| = 1$ for a perfect model. Linear regression plots including the stellar and planetary properties for all four ions are displayed in Appendix C.

moderate-to-high quality EUV spectra in the 90–360 Å range from *EUVE*. We use these samples to derive a tight relationship between the fractional FUV emission line luminosity and the fractional EUV luminosity. We present a new relationship for estimating ISM-corrected EUV irradiance in the 90–360 Å band, accurate to approximately a factor of 2, for low-mass stars with N V or Si IV spectra. EUV fluxes for each of our sample stars are given in Tables 3 and 4.

3. Comparing the FUV activity indices with a star–planet-interaction parameter ($M_{\text{plan}}/a_{\text{plan}}$), we found a significant correlation ($\sim 99\%$ confidence) between the presence of massive, short-period planets and stellar activity as indicated by enhanced FUV line emission. However, observational and astrophysical biases complicate the direct connection of the enhanced UV activity with the planetary system. We mitigated these interdependencies by creating a PCA treatment of the linear regression problem, finding that fits including SPI do not present a statistically better description of the observations. On the other hand, our observations do not conclusively rule out the influence of SPIs. Tides raised on the star by the orbiting planets could influence the stellar rotation period variations, but we do not observe correlations between the UV activity and tidal SPI strength proportionalities.

The data presented here were obtained as part of the *HST* Guest Observing programs #12464, #13650, and #14633. N.A. and K.F. thank Sebastian Pineda for an enjoyable discussion about the statistical analysis of this data set. We also acknowledge valuable discussions with Jeffrey Linsky. This work was supported by STScI grant HST-GO-14633.01. N.A. is supported by a NASA Earth and Space Sciences Fellowship (NESSF; 80NSSC17K0531) to the University of Colorado at Boulder. K.F. acknowledges the hospitality of the Reagan Test Site on Kwajalein Atoll, Republic of the Marshall Islands, where a portion of this work was carried out.

Appendix A

Si III, N V, C II, and Si IV Emission Line Measurements from the Planet-hosting and Non-planet-hosting Samples

In Tables 3 (planet-hosting stars) and 4 (non-planet hosts), we display the full emission line measurement lists for both samples studied in this work.

Appendix B

Si III, N V, C II, and Si IV Activity Levels versus $B - V$, Distance, and Rotation Period

In Figures 10–12 we show the correlation plots between the UV activity indices and $B - V$, d , and P_{rot} .

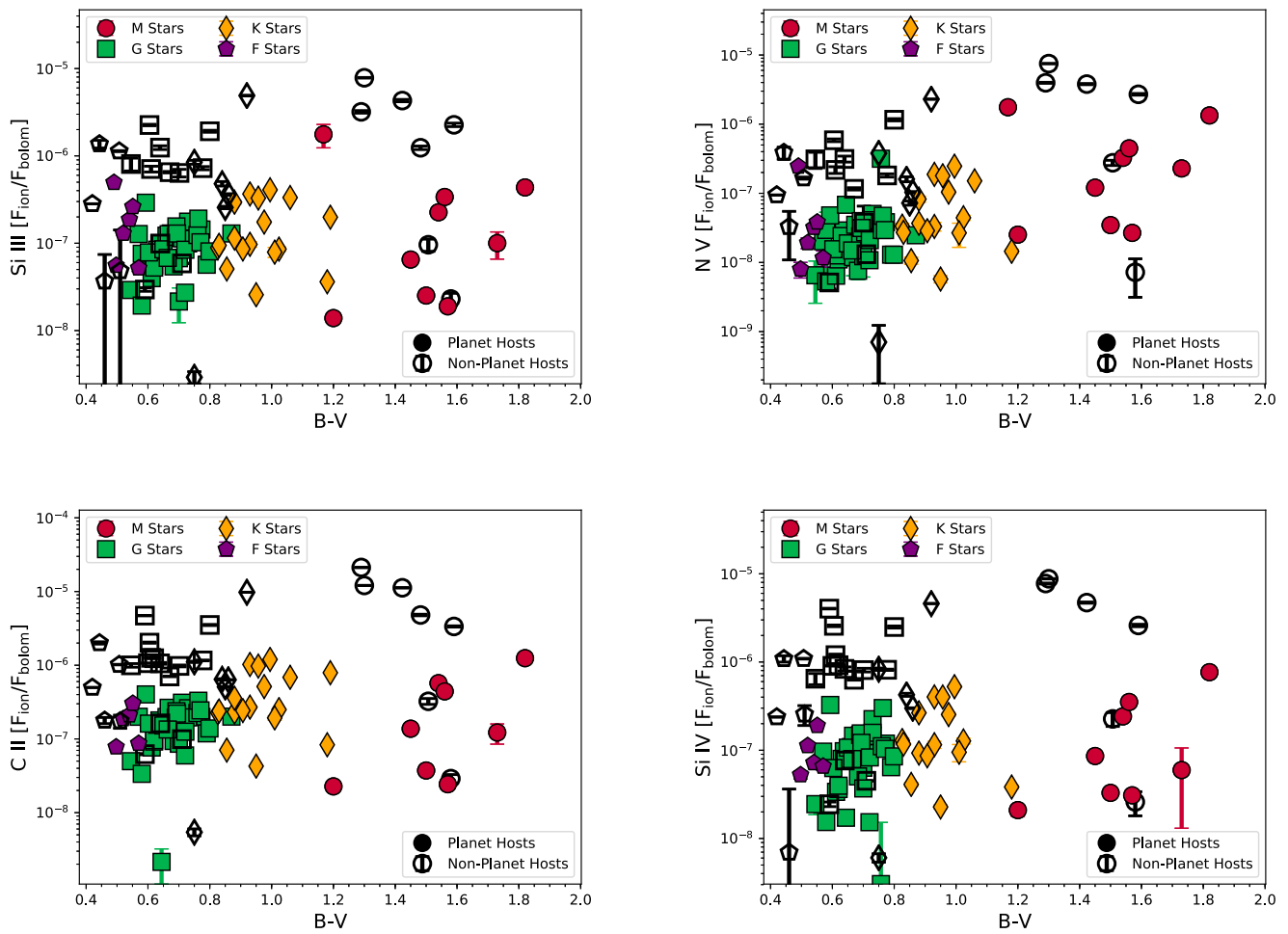


Figure 10. UV activity levels as a function of the spectral slope ($B-V$) for (top left to lower right) Si III λ 1206 Å, N V λ 1240 Å, C II λ 1335 Å, and Si IV λ 1400 Å. Spectral types are given by different symbols (circles: M dwarfs, diamonds: K dwarfs, squares: G dwarfs, pentagons: F dwarfs) as shown in the legend.

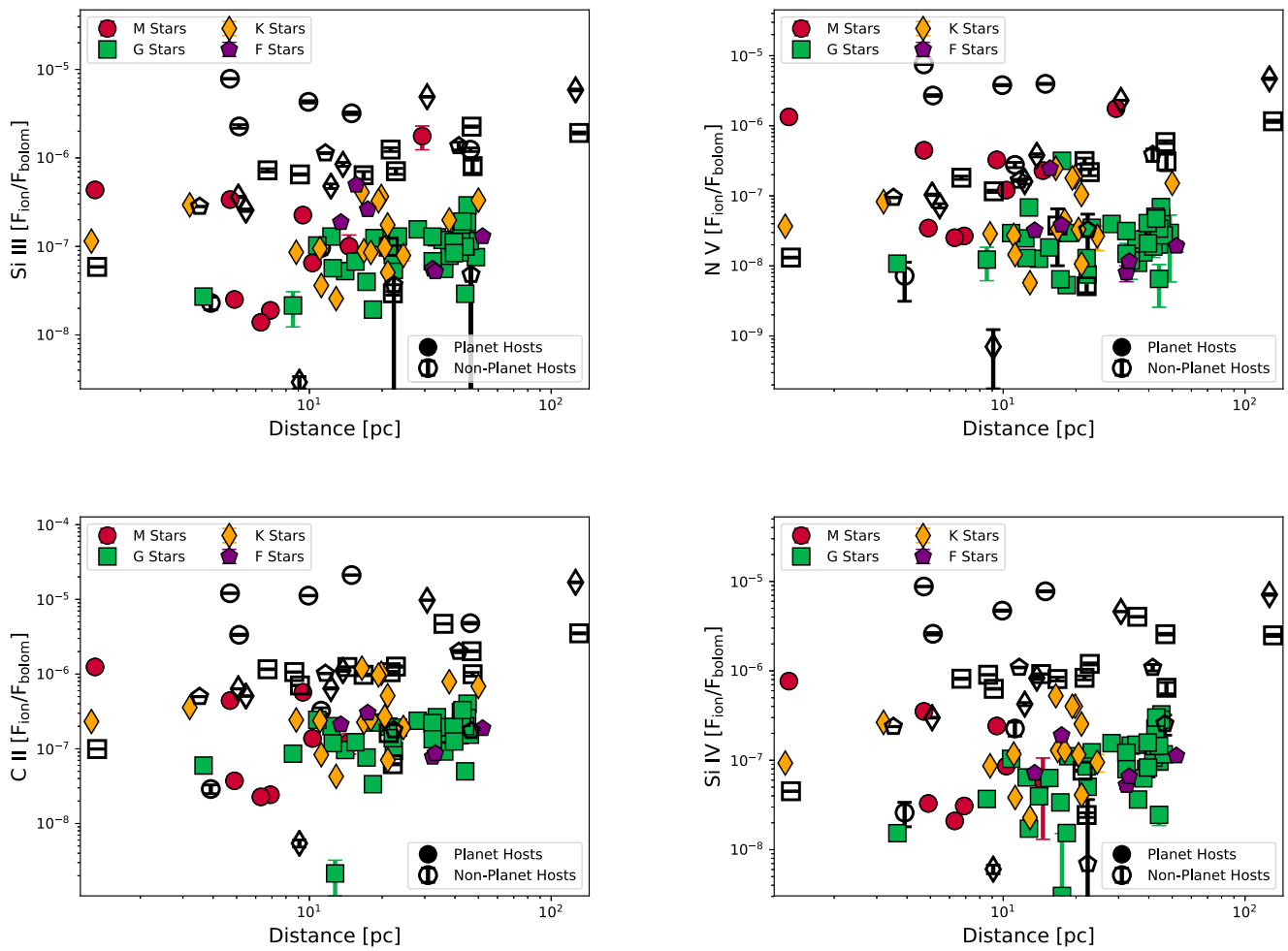


Figure 11. UV activity levels as a function of distance for (top left to lower right) Si III λ 1206 Å, N V λ 1240 Å, C II λ 1335 Å, and Si IV λ 1400 Å. Spectral types are given by different symbols (circles: M dwarfs, diamonds: K dwarfs, squares: G dwarfs, pentagons: F dwarfs), as shown in the legend.

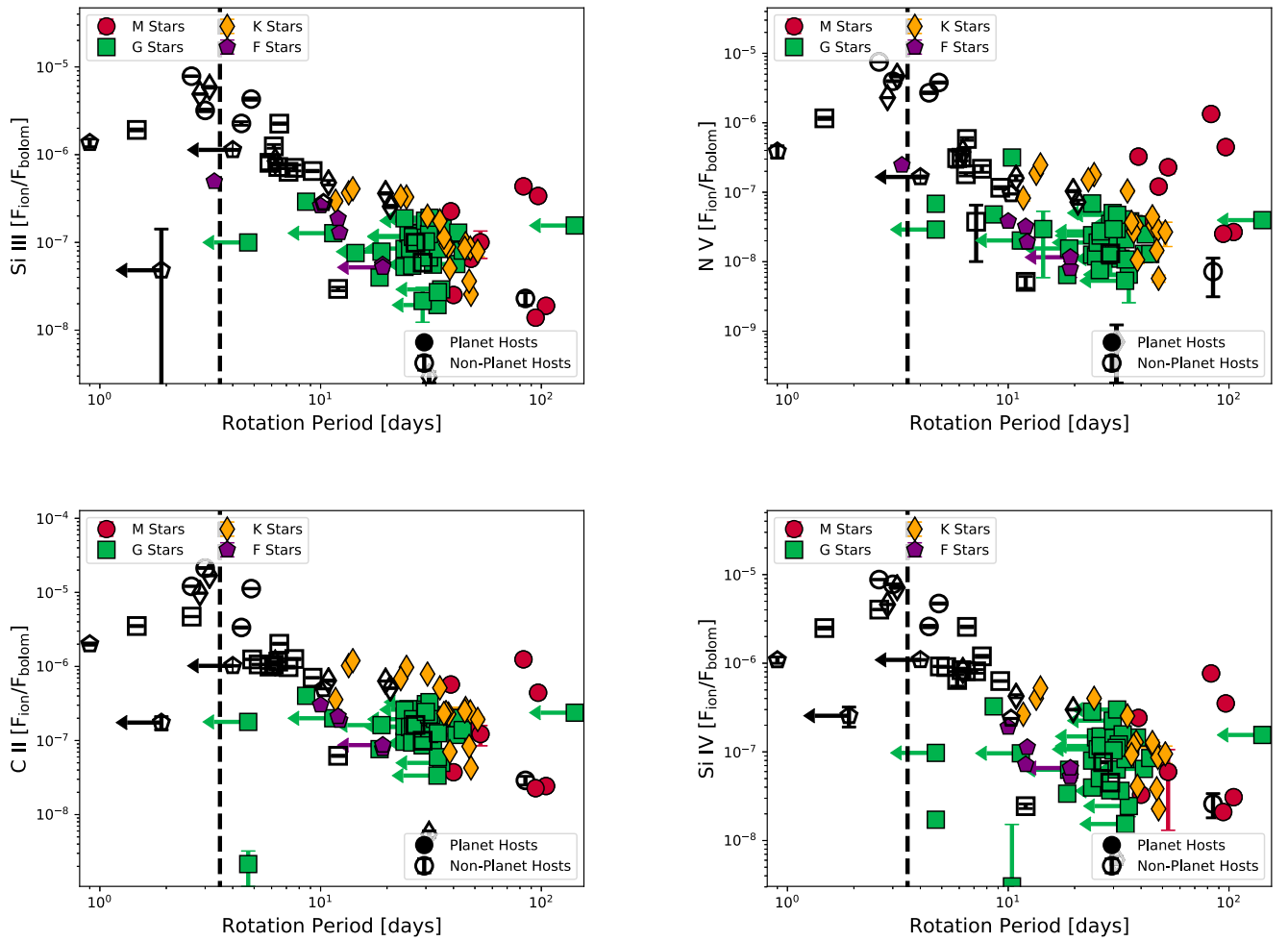


Figure 12. UV activity levels as a function of stellar rotation period (P_{rot}) for (top left to lower right) Si III λ 1206 Å, N V λ 1240 Å, C II λ 1335 Å, and Si IV λ 1400 Å. Spectral types are given by different symbols (circles: M dwarfs; diamonds: K dwarfs; squares: G dwarfs; pentagons: F dwarfs) as shown in the legend.

Appendix C PCA of Multivariate SPI Signals

In this appendix, we describe the methodology and calculations for the PCA analysis of the star–planet–interaction signal in our UV activity survey (see the overview in Section 4.2). First, the predictor variables must be centered and scaled as

$$\tilde{X}_{i,\text{scaled}} = \frac{x_i - \bar{x}}{L_x}, \quad L_x = \sqrt{\sum_{i=1}^n (x_i - \bar{x})^2}, \quad (7)$$

where each x_i is the predictor variable corresponding to an individual stellar system and \bar{x} is the average of the entire sample. The scaling simplifies the problem by allowing us to calculate the correlations between scaled parameters as

$$\text{Cor}(X_j, X_k) = \sum_{i=1}^n \tilde{X}_{ij,\text{scaled}} \tilde{X}_{ik,\text{scaled}}, \quad (8)$$

where the indices j and k represent predictor variables (e.g., j for $B - V$ and k for T_{eff}). We construct a matrix by calculating correlation coefficients between each set of scaled predictor variables:

	P_{rot}	V	$B - V$	d	T_{eff}	$\log(\text{SPI})$
P_{rot}	1	0.39	0.56	-0.34	-0.58	-0.26
V	0.39	1	0.67	0.17	-0.68	0.08
$B - V$	0.56	0.67	1	-0.48	-0.97	-0.20
d	-0.34	0.17	-0.48	1	0.52	0.35
T_{eff}	-0.58	-0.68	-0.97	0.52	1	0.20
$\log(\text{SPI})$	-0.26	0.08	-0.20	0.35	0.20	1

As expected, each parameter is perfectly correlated with itself, as evidenced by the coefficients of 1 along the diagonal of the correlation matrix. Next, we calculate the eigenvalues of the correlation matrix and place them in descending order ($\lambda = 3.22, 1.41, 0.72, 0.54, 0.085, 0.026$), where the largest eigenvalue is associated with the PC that contributes most to the spread of fractional luminosities. The PCs can be constructed from the eigenvectors of the correlation matrix,

Table 7
Correlations between Stellar Parameters and Principal Components: Planet Hosts

	PC ₁		PC ₂		PC ₃		PC ₄		PC ₅		PC ₆	
	ρ	p -value	ρ	p -value	ρ	p -value	ρ	p -value	ρ	p -value	ρ	p -value
P_{rot}	-0.798	2×10^{-16}	-0.144	0.2	-0.165	0.2	0.287	0.02	0.190	0.1	-0.0128	0.9
V	-0.455	9×10^{-5}	0.653	1×10^{-9}	-0.256	0.03	-0.173	0.2	0.293	0.01	0.0948	0.4
$B - V$	-0.929	2×10^{-30}	-0.0144	0.9	0.160	0.2	-0.168	0.2	0.354	0.003	0.0152	0.9
d	0.558	6×10^{-7}	0.654	1×10^{-9}	-0.522	4×10^{-6}	0.0368	0.8	0.120	0.3	-0.0407	0.7
T_{eff}	0.927	3×10^{-30}	0.0807	0.5	-0.199	0.1	0.189	0.1	-0.285	0.02	0.136	0.3
$\log(\text{SPI})$	0.397	7×10^{-4}	0.694	4×10^{-11}	0.512	7×10^{-6}	0.410	5×10^{-4}	0.00216	0.986	-0.0449	0.7

Note. ρ is the Spearman rank coefficient, where $|\rho| = 1$ for a perfect correlation and $\rho = 0$ when the data are uncorrelated. The p -value indicates the likelihood of obtaining $|\rho|$ closer to 1, under the assumption that there is no correlation between the two parameters (i.e., the data are randomly distributed). Here, we define “significant” correlations here as having $|\rho| > 0.5$ (marked in bold).

in order from most to least significant:

$$\begin{aligned}
 \text{PC}_1 &= -0.41 \times P_{\text{rot, scaled}} - 0.37 \times V_{\text{scaled}} \\
 &\quad - 0.53 \times (B - V)_{\text{scaled}} \\
 &\quad + 0.30 \times d_{\text{scaled}} + 0.54 \times T_{\text{eff, scaled}} \\
 &\quad + 0.18 \times \log(\text{SPI})_{\text{scaled}} \\
 \text{PC}_2 &= -0.059 \times P_{\text{rot, scaled}} + 0.58 \times V_{\text{scaled}} \\
 &\quad + 0.089 \times (B - V)_{\text{scaled}} \\
 &\quad + 0.58 \times d_{\text{scaled}} - 0.077 \times T_{\text{eff, scaled}} \\
 &\quad + 0.57 \times \log(\text{SPI})_{\text{scaled}} \\
 \text{PC}_3 &= -0.26 \times P_{\text{rot, scaled}} - 0.24 \times V_{\text{scaled}} \\
 &\quad + 0.14 \times (B - V)_{\text{scaled}} \\
 &\quad - 0.55 \times d_{\text{scaled}} - 0.16 \times T_{\text{eff, scaled}} \\
 &\quad + 0.73 \times \log(\text{SPI})_{\text{scaled}} \\
 \text{PC}_4 &= 0.87 \times P_{\text{rot, scaled}} - 0.20 \times V_{\text{scaled}} \\
 &\quad - 0.22 \times (B - V)_{\text{scaled}} \\
 &\quad + 0.0083 \times d_{\text{scaled}} + 0.19 \times T_{\text{eff, scaled}} \\
 &\quad + 0.34 \times \log(\text{SPI})_{\text{scaled}} \\
 \text{PC}_5 &= 0.017 \times P_{\text{rot, scaled}} - 0.64 \times V_{\text{scaled}} \\
 &\quad + 0.56 \times (B - V)_{\text{scaled}} \\
 &\quad + 0.50 \times d_{\text{scaled}} - 0.16 \times T_{\text{eff, scaled}} \\
 &\quad + 0.030 \times \log(\text{SPI})_{\text{scaled}} \\
 \text{PC}_6 &= 0.012 \times P_{\text{rot, scaled}} + 0.18 \times V_{\text{scaled}} \\
 &\quad + 0.57 \times (B - V)_{\text{scaled}} \\
 &\quad - 0.16 \times d_{\text{scaled}} + 0.79 \times T_{\text{eff, scaled}} \\
 &\quad + 0.00026 \times \log(\text{SPI})_{\text{scaled}}. \tag{9}
 \end{aligned}$$

Although it is difficult to quantify the contribution of the individual predictor variables to each PC, we can get a rough sense of which are significant by calculating the Spearman rank coefficients (see Table 7). We find that the most dominant PC (PC₁) is significantly correlated with P_{rot} , $B - V$, d , and T_{eff} . The SPI parameter is only weakly correlated with PC₁, but it contributes more to PC₂ and PC₃, which show smaller correlations with the other stellar parameters. PC₄, PC₅, and PC₆ are not strongly correlated with any of the predictor variables, indicating that they contribute less to the multiple linear regression and can be dropped from the analysis (Peres-Neto et al. 2005). The new

Table 8
Multiple Linear Regression Results: Principal Components as Predictor Variables for Planet Hosts

Element	Predictor Variable	β	95% Confidence Interval
N V	PC ₁	-0.2516	(-0.356, -0.147)
	PC ₂	0.3193	(0.123, 0.516)
	PC ₃	0.3928	(0.166, 0.620)
	y-intercept	-0.0092	(-0.032, 0.014)
	ρ	0.581	$p = 1 \times 10^{-6}$
Si III	PC ₁	0.0562	(-0.071, 0.184)
	PC ₂	0.2424	(0.005, 0.480)
	PC ₃	0.3029	(0.024, 0.582)
	y-intercept	-0.0067	(-0.035, 0.021)
	ρ	0.370	$p = 3 \times 10^{-3}$
Si IV	PC ₁	-0.0012	(-0.158, 0.156)
	PC ₂	0.288	(-0.022, 0.598)
	PC ₃	0.252	(-0.115, 0.619)
	y-intercept	0.0008	(-0.034, 0.035)
	ρ	0.325	$p = 0.01$
C II	PC ₁	0.0307	(-0.122, 0.183)
	PC ₂	0.268	(-0.010, 0.546)
	PC ₃	0.309	(-0.047, 0.665)
	y-intercept	0.0027	(-0.030, 0.036)
	ρ	0.327	$p = 0.01$

Note. ρ is the Spearman rank coefficient, calculated between the multiple linear regression model and the observed fractional luminosities in a given element.

linear model becomes

$$\begin{aligned}
 \log(L_{\text{ion}}/L_{\text{bol}}) &= \beta_0 + [\text{PC}_1 \times \beta_{\text{PC}_1}] \\
 &\quad + [\text{PC}_2 \times \beta_{\text{PC}_2}] + [\text{PC}_3 \times \beta_{\text{PC}_3}]. \tag{10}
 \end{aligned}$$

Table 8 lists the coefficients (β) of the multiple linear regression analysis described by Equation (10). Figure 13 displays the Spearman rank coefficients for the planet-hosting sample.

C.1. Non-planet Hosts

The same analysis that we carried out for the planet-hosting stars was also applied to the sample of non-planet hosts, with the SPI parameter dropped as a predictor variable. The resulting

Table 9
Correlations between Stellar Parameters and Principal Components: Non-planet Hosts

	PC ₁		PC ₂		PC ₃		PC ₄		PC ₅	
	ρ	p -value	ρ	p -value	ρ	p -value	ρ	p -value	ρ	p -value
P_{rot}	0.796	1×10^{-7}	-0.133	0.5	-0.552	0.002	-0.566	0.001	-0.0260	0.9
V	-0.365	0.05	-0.312	0.09	-0.187	0.3	0.180	0.3	-0.458	0.01
$B - V$	0.230	0.2	-0.868	5×10^{-10}	0.287	0.1	-0.170	0.4	0.128	0.5
d	-0.901	1×10^{-11}	0.381	0.04	-0.269	0.2	-0.141	0.5	-0.421	0.02
T_{eff}	-0.471	0.009	0.905	7×10^{-12}	-0.0376	0.8	-0.0109	0.9	-0.0245	0.9

Note. ρ is the Spearman rank coefficient, where $|\rho| = 1$ for a perfect correlation and $\rho = 0$ when the data are uncorrelated. The p -value indicates the likelihood of obtaining $|\rho|$ closer to 1, under the assumption that there is no correlation between the two parameters (i.e., the data are randomly distributed). Here we define “significant” correlations here as having $|\rho| > 0.5$ (marked in bold).

correlation matrix, calculated from the scaled parameters, is

$$\begin{array}{c} P_{\text{rot}} \\ V \\ B - V \\ d \\ T_{\text{eff}} \end{array} \begin{array}{c} P_{\text{rot}} \\ V \\ B - V \\ d \\ T_{\text{eff}} \end{array} \begin{bmatrix} 1 & -0.25 & -0.20 & -0.59 & -0.22 \\ -0.25 & 1 & 0.14 & 0.52 & -0.33 \\ -0.20 & 0.14 & 1 & -0.055 & -0.40 \\ -0.59 & 0.52 & -0.055 & 1 & 0.30 \\ -0.22 & -0.33 & -0.40 & 0.30 & 1 \end{bmatrix},$$

corresponding to eigenvalues [1.96, 1.58, 0.90, 0.36, 0.20] and principal components:

$$\begin{aligned}
 \text{PC}_1 &= 0.58 \times P_{\text{rot, scaled}} - 0.47 \times V_{\text{scaled}} \\
 &\quad - 0.09 \times (B - V)_{\text{scaled}} \\
 &\quad - 0.65 \times d_{\text{scaled}} - 0.14 \times T_{\text{eff, scaled}} \\
 \text{PC}_2 &= -0.06 \times P_{\text{rot, scaled}} - 0.38 \times V_{\text{scaled}} \\
 &\quad - 0.57 \times (B - V)_{\text{scaled}} \\
 &\quad + 0.15 \times d_{\text{scaled}} + 0.71 \times T_{\text{eff, scaled}} \\
 \text{PC}_3 &= -0.46 \times P_{\text{rot, scaled}} - 0.55 \times V_{\text{scaled}} \\
 &\quad + 0.65 \times (B - V)_{\text{scaled}} \\
 &\quad - 0.14 \times d_{\text{scaled}} + 0.22 \times T_{\text{eff, scaled}} \\
 \text{PC}_4 &= -0.65 \times P_{\text{rot, scaled}} - 0.14 \times V_{\text{scaled}} \\
 &\quad - 0.49 \times (B - V)_{\text{scaled}} \\
 &\quad - 0.31 \times d_{\text{scaled}} - 0.47 \times T_{\text{eff, scaled}} \\
 \text{PC}_5 &= -0.17 \times P_{\text{rot, scaled}} + 0.56 \times V_{\text{scaled}} \\
 &\quad + 0.05 \times (B - V)_{\text{scaled}} \\
 &\quad - 0.66 \times d_{\text{scaled}} + 0.46 \times T_{\text{eff, scaled}}. \tag{11}
 \end{aligned}$$

Table 9 lists the correlation coefficients between the PCs and the stellar parameters. The first PC is strongly correlated with P_{rot} and d , while $B - V$ and T_{eff} are more significant in PC₂. P_{rot} alone is also correlated with PC₃ and PC₄. We drop PC₅ from the regression analysis, since this component is not strongly correlated with any of the stellar parameters, and find that the linear model appears to describe the sample of non-planet hosts better than the sample of planet hosts. We find larger Spearman rank coefficients between the models and

Table 10

Multiple Linear Regression Results: Principal Components as Predictor Variables for Non-Planet Hosts

Element	Predictor Variable	β	95% Confidence Interval
N v	PC ₁	-0.5461	(-0.810, -0.282)
	PC ₂	-0.3460	(-0.578, -0.114)
	PC ₃	0.8376	(0.047, 1.628)
	PC ₄	0.4471	(-0.327, 1.221)
	y-intercept	-0.0161	(-0.068, 0.036)
	ρ	0.897	$p = 3 \times 10^{-9}$
Si III	PC ₁	-0.4578	(-0.782, -0.134)
	PC ₂	-0.2470	(-0.527, 0.033)
	PC ₃	0.7144	(-0.253, 1.682)
	PC ₄	0.2960	(-0.639, 1.231)
	y-intercept	-0.0029	(-0.065, 0.059)
	ρ	0.831	$p = 1 \times 10^{-7}$
Si IV	PC ₁	-0.4907	(-0.739, -0.242)
	PC ₂	-0.2423	(-0.452, -0.033)
	PC ₃	0.6423	(-0.093, 1.377)
	PC ₄	0.3728	(-0.326, 1.071)
	y-intercept	-0.0019	(-0.047, 0.043)
	ρ	0.833	$p = 4 \times 10^{-8}$
C II	PC ₁	-0.4987	(-0.761, -0.237)
	PC ₂	-0.2831	(-0.508, -0.058)
	PC ₃	0.8234	(0.042, 1.605)
	PC ₄	0.2921	(-0.457, 1.041)
	y-intercept	-0.0165	(-0.064, 0.031)
	ρ	0.846	$p = 7 \times 10^{-9}$

Note. ρ is the Spearman rank coefficient, calculated between the multiple linear regression model and the observed fractional luminosities in a given element.

observed fractional luminosities for all four elements (see Table 10) in the non-planet hosts than in the planet-hosting sample. Both PC₁ and PC₂ contribute significantly to the spread in the data for all ions except Si III, again in contrast with the planet-hosting sample.

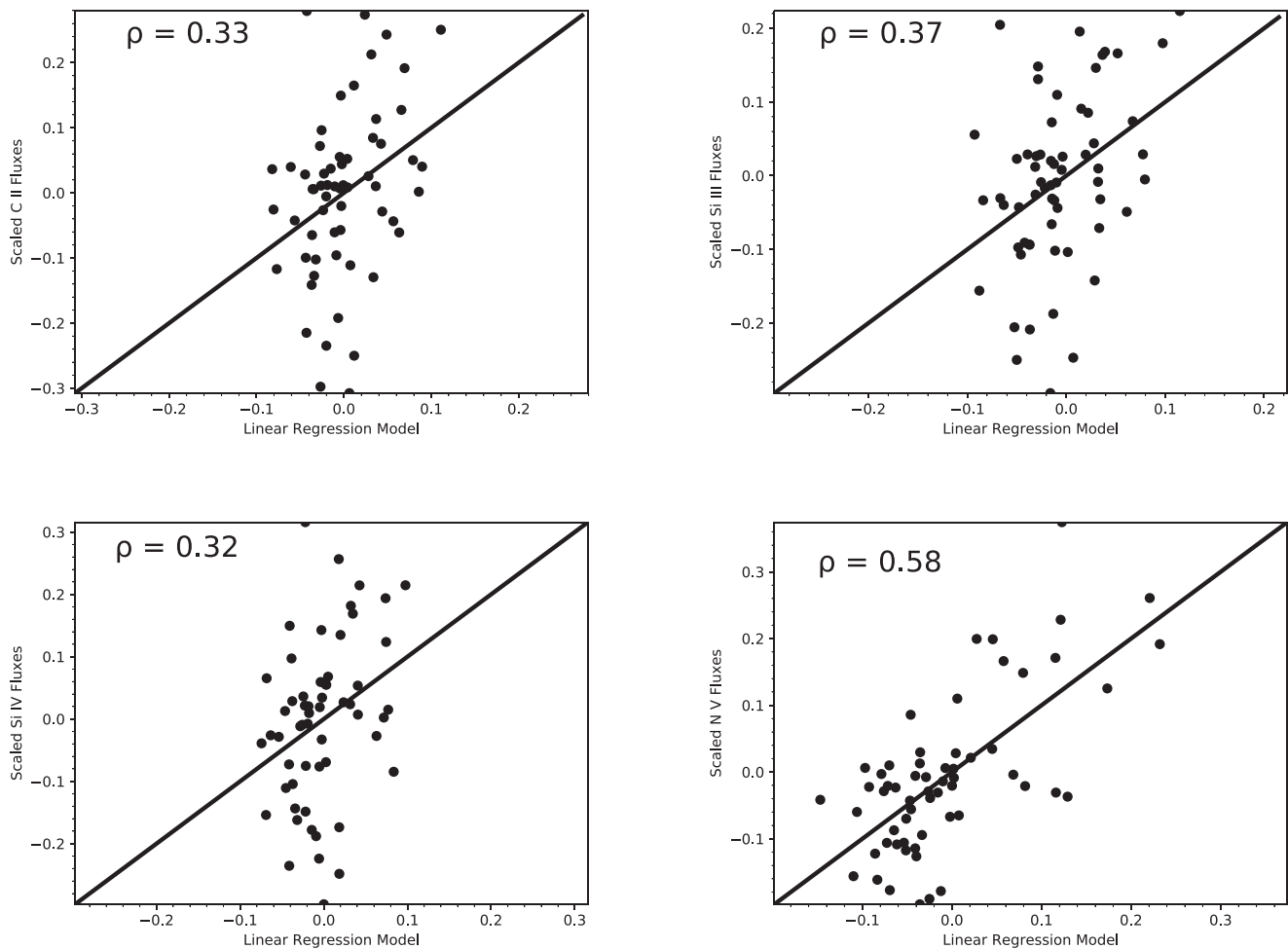


Figure 13. Comparison of the linear regression model and relative ion fluxes for planet-hosting stars. The Spearman correlation coefficient (ρ) describes the agreement between the multivariate linear model and our observations, where we expect $|\rho| = 1$ for a perfect model. Linear regression plots for all four ions are displayed in Appendix C.

ORCID iDs

Kevin France <https://orcid.org/0000-0002-1002-3674>
 Nicole Arulanantham <https://orcid.org/0000-0003-2631-5265>
 Luca Fossati <https://orcid.org/0000-0003-4426-9530>
 Antonino F. Lanza <https://orcid.org/0000-0001-5928-7251>
 R. O. Parke Loyd <https://orcid.org/0000-0001-5646-6668>
 Seth Redfield <https://orcid.org/0000-0003-3786-3486>

References

- Adams, F. C. 2011, *ApJ*, **730**, 27
 Airapetian, V. S., Gloer, A., Khazanov, G. V., et al. 2017, *ApJL*, **836**, L3
 Ammler-von Eiff, M., & Reiners, A. 2012, *A&A*, **542**, A116
 Anderson, D. R., Collier Cameron, A., Delrez, L., et al. 2014, *MNRAS*, **445**, 1114
 Anglada-Escudé, G., Amado, P. J., Barnes, J., et al. 2016, *Natur*, **536**, 437
 Arentoft, T., Kjeldsen, H., Bedding, T. R., et al. 2008, *ApJ*, **687**, 1180
 Ayres, T. R. 1997, *JGR*, **102**, 1641
 Ayres, T. R. 2010, *ApJS*, **187**, 149
 Baines, E. K., McAlister, H. A., ten Brummelaar, T. A., et al. 2008, *ApJ*, **680**, 728
 Bakos, G. Á., Torres, G., Pál, A., et al. 2010, *ApJ*, **710**, 1724
 Baliunas, S., Sokoloff, D., & Soon, W. 1996, *ApJL*, **457**, L99
 Baliunas, S. L., Henry, G. W., Donahue, R. A., Fekel, F. C., & Soon, W. H. 1997, *ApJL*, **474**, L119
 Balona, L. A. 2012, *MNRAS*, **423**, 3420
 Bastian, T. S., Dulk, G. A., & Leblanc, Y. 2000, *ApJ*, **545**, 1058
 Bastian, T. S., Villadsen, J., Maps, A., Hallinan, G., & Beasley, A. J. 2018, *ApJ*, **857**, 133
 Belu, A. R., Selsis, F., Morales, J.-C., et al. 2011, *A&A*, **525**, A83
 Ben-Jaffel, L., & Ballester, G. E. 2013, *A&A*, **553**, A52
 Berdyugina, S. V. 2005, *LRSP*, **2**, 8
 Boesgaard, A. M., Lum, M. G., Deliyannis, C. P., et al. 2016, *ApJ*, **830**, 49
 Bonfanti, A., Ortolani, S., Piotto, G., & Nascimbeni, V. 2015, *A&A*, **575**, A18
 Bonfils, X., Gillon, M., Udry, S., et al. 2012, *A&A*, **546**, A27
 Booth, R. S., Poppenhaeger, K., Watson, C. A., Silva Aguirre, V., & Wolk, S. J. 2017, *MNRAS*, **471**, 1012
 Bouchy, F., Mayor, M., Lovis, C., et al. 2009, *A&A*, **496**, 527
 Bourrier, V., & Lecavelier des Etangs, A. 2013, *A&A*, **557**, A124
 Brandenburg, A., Mathur, S., & Metcalfe, T. S. 2017, *ApJ*, **845**, 79
 Brown, D. J. A. 2014, *MNRAS*, **442**, 1844
 Brown, T. M., Charbonneau, D., Gilliland, R. L., Noyes, R. W., & Burrows, A. 2001, *ApJ*, **552**, 699
 Brown, T. M., Latham, D. W., Everett, M. E., & Esquerdo, G. A. 2011, *AJ*, **142**, 112
 Buchhave, L. A., & Latham, D. W. 2015, *ApJ*, **808**, 187
 Butler, R. P., Marcy, G. W., Fischer, D. A., et al. 1999, *ApJ*, **526**, 916
 Castell, F., & Kurucz, R. L. 2004, arXiv:astro-ph/0405087
 Cauley, P. W., Redfield, S., Jensen, A. G., et al. 2015, *ApJ*, **810**, 13
 Chabrier, G., & Baraffe, I. 1995, *ApJL*, **451**, L29
 Christensen, U. R., Holzwarth, V., & Reiners, A. 2009, *Natur*, **457**, 167
 Christian, D. J., Mathioudakis, M., Bloomfield, D. S., Dupuis, J., & Keenan, F. P. 2004, *ApJ*, **612**, 1140
 Cockell, C. S., Bush, T., Bryce, C., et al. 2016, *AsBio*, **16**, 89
 Craig, N., Abbott, M., Finley, D., et al. 1997, *ApJS*, **113**, 131
 Cuntz, M., Saar, S. H., & Musielak, Z. E. 2000, *ApJL*, **533**, L151
 da Silva, R., Milone, A. D. C., & Rocha-Pinto, H. J. 2015, *A&A*, **580**, A24

- Deming, D., Seager, S., Winn, J., et al. 2009, *PASP*, **121**, 952
- Dere, K. P., Landi, E., Young, P. R., et al. 2009, *A&A*, **498**, 915
- deWarf, L. E., Datin, K. M., & Guinan, E. F. 2010, *ApJ*, **722**, 343
- do Nascimento, J.-D., Jr., Vidotto, A. A., Petit, P., et al. 2016, *ApJL*, **820**, L15
- Donahue, R. A., Saar, S. H., & Baliunas, S. L. 1996, *ApJ*, **466**, 384
- Dupuis, J., Vennes, S., Bowyer, S., Pradhan, A. K., & Thejll, P. 1995, *ApJ*, **455**, 574
- Ehrenreich, D., Bourrier, V., Bonfils, X., et al. 2012, *A&A*, **547**, A18
- Ehrenreich, D., Bourrier, V., Wheatley, P. J., et al. 2015, *Natur*, **522**, 459
- Eisenbeiss, T., Ammler-von Eiff, M., Roell, T., et al. 2013, *A&A*, **556**, A53
- Fekel, F. C., Jr. 1983, *ApJ*, **268**, 274
- Fichtinger, B., Güdel, M., Mutel, R. L., et al. 2017, *A&A*, **599**, A127
- Fischer, D. A., Marcy, G. W., Butler, R. P., et al. 2001, *ApJ*, **551**, 1107
- Fischer, D. A., Marcy, G. W., Butler, R. P., et al. 2002, *PASP*, **114**, 529
- Fischer, D. A., Marcy, G. W., Butler, R. P., et al. 2003, *ApJ*, **586**, 1394
- Fontenla, J. M., Harder, J., Livingston, W., Snow, M., & Woods, T. 2011, *JGRD*, **116**, 20108
- Fontenla, J. M., Linsky, J. L., Witbrod, J., et al. 2016, *ApJ*, **830**, 154
- Foreman-Mackey, D., Hogg, D. W., Lang, D., & Goodman, J. 2013, *PASP*, **125**, 306
- Fossati, L., Haswell, C. A., Froning, C. S., et al. 2010, *ApJL*, **714**, L222
- Fossati, L., Koskinen, T., France, K., et al. 2018, *AJ*, **155**, 113
- France, K. 2016, *Proc. SPIE*, **9904**, 99040M
- France, K., Linsky, J. L., Tian, F., Froning, C. S., & Roberge, A. 2012, *ApJL*, **750**, L32
- France, K., Loyd, R. O. P., Youngblood, A., et al. 2016a, *ApJ*, **820**, 89
- France, K., Parke Loyd, R. O., Youngblood, A., et al. 2016b, *ApJ*, **820**, 89
- France, K., Stocke, J. T., Yang, H., et al. 2010, *ApJ*, **712**, 1277
- Fuhrmann, K., & Bernkopf, J. 2008, *MNRAS*, **384**, 1563
- Fuhrmann, K., Pfeiffer, M. J., & Bernkopf, J. 1997, *A&A*, **326**, 1081
- Fuhrmann, K., Pfeiffer, M. J., & Bernkopf, J. 1998, *A&A*, **336**, 942
- Fulton, B. J., Howard, A. W., Weiss, L. M., et al. 2016, *ApJ*, **830**, 46
- Gaidos, E. J., & Gonzalez, G. 2002, *NewA*, **7**, 211
- Gaidos, E. J., Henry, G. W., & Henry, S. M. 2000, *AJ*, **120**, 1006
- Garraffo, C., Drake, J. J., & Cohen, O. 2016, *ApJL*, **833**, L4
- Ge, Z. S., Bi, S. L., Chen, Y. Q., et al. 2016, *ApJ*, **833**, 161
- Gray, D. F. 1994, *PASP*, **106**, 1248
- Grieffmeier, J.-M. 2015, *AASL*, **411**, 213
- Guinan, E. F., Engle, S. G., & Durbin, A. 2016, *ApJ*, **821**, 81
- Hale, A. 1994, *AJ*, **107**, 306
- Hallam, K. L., Altner, B., & Endal, A. S. 1991, *ApJ*, **372**, 610
- Hallinan, G., Sirothia, S. K., Antonova, A., et al. 2013, *ApJ*, **762**, 34
- Harman, C. E., Schwieterman, E. W., Schottelkotte, J. C., & Kasting, J. F. 2015, *ApJ*, **812**, 137
- Hempelmann, A., Schmitt, J. H. M. M., Schultz, M., Ruediger, G., & Stepien, K. 1995, *A&A*, **294**, 515
- Henry, G. W., Donahue, R. A., & Baliunas, S. L. 2002, *ApJL*, **577**, L111
- Houdebine, E. R. 2010, *MNRAS*, **407**, 1657
- Howard, A. W., Johnson, J. A., Marcy, G. W., et al. 2009, *ApJ*, **696**, 75
- Howard, A. W., Johnson, J. A., Marcy, G. W., et al. 2011, *ApJ*, **726**, 73
- Huang, Y., Liu, X.-W., Yuan, H.-B., et al. 2015, *MNRAS*, **454**, 2863
- Husser, T.-O., Wende-von Berg, S., Dreizler, S., et al. 2013, *A&A*, **553**, A6
- Ignace, R., Giroux, M. L., & Luttermoser, D. G. 2010, *MNRAS*, **402**, 2609
- Isaacson, H., & Fischer, D. 2010, *ApJ*, **725**, 875
- Jones, B. W., & Sleep, P. N. 2010, *MNRAS*, **407**, 1259
- Jones, H. R. A., Butler, R. P., Tinney, C. G., et al. 2006, *MNRAS*, **369**, 249
- Kajatkari, P., Jetsu, L., Cole, E., et al. 2015, *A&A*, **577**, A84
- Kervella, P., Thévenin, F., Ségransan, D., et al. 2003, *A&A*, **404**, 1087
- Kiraga, M. 2012, *AcA*, **62**, 67
- Knutson, H. A., Charbonneau, D., Allen, L. E., et al. 2007, *Natur*, **447**, 183
- Koskinen, T. T., Harris, M. J., Yelle, R. V., & Lavvas, P. 2013, *Icar*, **226**, 1678
- Kruczek, N., France, K., Evonosky, W., et al. 2017, *ApJ*, **845**, 3
- Lammer, H., Güdel, M., Kulikov, Y., et al. 2012, *EP&S*, **64**, 179
- Lammer, H., Odert, P., Leitzinger, M., et al. 2009, *A&A*, **506**, 399
- Lammer, H., Zerkle, A. L., Gebauer, S., et al. 2018, *A&ARv*, **26**, 2
- Lanza, A. F. 2008, *A&A*, **487**, 1163
- Lanza, A. F. 2010, *A&A*, **512**, A77
- Lanza, A. F. 2012, *A&A*, **544**, A23
- Lanza, A. F. 2013, *A&A*, **557**, A31
- Lanza, A. F. 2015, in 18th Cambridge Workshop on Cool Stars, Stellar Systems, and the Sun, ed. G. T. van Belle & H. C. Harris (Cambridge: Cambridge Univ. Press), 811
- Lanza, A. F. 2018, *A&A*, **610**, A81
- Lazio, J., Farrell, W. M., Dietrick, J., et al. 2004, arXiv:astro-ph/0405343
- Lecavelier des Etangs, A., Sirothia, S. K., Gopal-Krishna, & Zarka, P. 2013, *A&A*, **552**, A65
- Liddle, A. R. 2007, *MNRAS*, **377**, L74
- Linsky, J. L., Bushinsky, R., Ayres, T., Fontenla, J., & France, K. 2012a, *ApJ*, **745**, 25
- Linsky, J. L., Bushinsky, R., Ayres, T., & France, K. 2012b, *ApJ*, **754**, 69
- Linsky, J. L., Fontenla, J., & France, K. 2014, *ApJ*, **780**, 61
- Linsky, J. L., Yang, H., France, K., et al. 2010, *ApJ*, **717**, 1291
- Lopez, E. D., & Fortney, J. J. 2013, *ApJ*, **776**, 2
- Louden, T., Wheatley, P. J., & Briggs, K. 2017, *MNRAS*, **464**, 2396
- Lovis, C., Dumusque, X., Santos, N. C., et al. 2011, arXiv:1107.5325
- Lovis, C., Mayor, M., Bouchy, F., et al. 2005, *A&A*, **437**, 1121
- Lovis, C., Mayor, M., Pepe, F., et al. 2006, *Natur*, **441**, 305
- Loyd, R. O. P., & France, K. 2014, *ApJS*, **211**, 9
- Loyd, R. O. P., France, K., Youngblood, A., et al. 2016, *ApJ*, **824**, 102
- Loyd, R. O. P., Koskinen, T. T., France, K., Schneider, C., & Redfield, S. 2017, *ApJL*, **834**, L17
- Maldonado, J., Scandariato, G., Stelzer, B., et al. 2017, *A&A*, **598**, A27
- Malo, L., Artigau, É., Doyon, R., et al. 2014, *ApJ*, **788**, 81
- Mann, A. W., Feiden, G. A., Gaidos, E., Boyajian, T., & von Braun, K. 2015, *ApJ*, **804**, 64
- Marcy, G. W., Butler, R. P., Fischer, D. A., & Vogt, S. S. 2004, in ASP Conf. Ser. 321, Extrasolar Planets: Today and Tomorrow, ed. J. Beaulieu, A. Lecavelier Des Etangs, & C. Terquem (San Francisco, CA: ASP), 3
- Marmier, M., Ségransan, D., Udry, S., et al. 2013, *A&A*, **551**, A90
- Maxted, P. F. L., Serenelli, A. M., & Southworth, J. 2015, *A&A*, **577**, A90
- Mayor, M., Udry, S., Naef, D., et al. 2004, *A&A*, **415**, 391
- Mazeh, T., Naef, D., Torres, G., et al. 2000, *ApJL*, **532**, L55
- Menager, H., Barthélemy, M., Koskinen, T., Lilensten, J., Ehrenreich, D., & Parkinson, C. D. 2013, *Icar*, **226**, 1709
- Mennesson, B., Gaudi, S., Seager, S., et al. 2016, *Proc. SPIE*, **9904**, 99040L
- Meschiari, S., Laughlin, G., Vogt, S. S., et al. 2011, *ApJ*, **727**, 117
- Messina, S., Desidera, S., Turatto, M., Lanzafame, A. C., & Guinan, E. F. 2010, *A&A*, **520**, A15
- Miller, B. P., Gallo, E., Wright, J. T., & Pearson, E. G. 2015, *ApJ*, **799**, 163
- Mordasini, C., Mayor, M., Udry, S., et al. 2011, *A&A*, **526**, A111
- Moutou, C., Hébrard, G., Bouchy, F., et al. 2014, *A&A*, **563**, A22
- Murray-Clay, R. A., Chiang, E. I., & Murray, N. 2009, *ApJ*, **693**, 23
- Naef, D., Mayor, M., Pepe, F., et al. 2000, in ASP Conf. Ser. 219, Disks, Planetesimals, and Planets, ed. G. Garzón et al. (San Francisco, CA: ASP), 602
- Neves, V., Bonfils, X., Santos, N. C., et al. 2013, *A&A*, **551**, A36
- Newton, E. R., Irwin, J., Charbonneau, D., et al. 2016, *ApJ*, **821**, 93
- Newton, E. R., Irwin, J., Charbonneau, D., et al. 2017, *ApJ*, **834**, 85
- Nordström, B., Mayor, M., Andersen, J., et al. 2004, *A&A*, **418**, 989
- Noyes, R. W., Hartmann, L. W., Baliunas, S. L., Duncan, D. K., & Vaughan, A. H. 1984, *ApJ*, **279**, 763
- Olsper, N., Lehtinen, J. J., Käpylä, M. J., Pelt, J., & Grigorievskiy, A. 2018, *A&A*, **619**, A6
- Owen, J. E., & Wu, Y. 2013, *ApJ*, **775**, 105
- Pawellek, N., Krivov, A. V., Marshall, J. P., et al. 2014, *ApJ*, **792**, 65
- Pearson, K. 1901, *PMag*, **11**, 559
- Pecaut, M. J., & Mamajek, E. E. 2013, *ApJS*, **208**, 9
- Pepe, F., Lovis, C., Ségransan, D., et al. 2011, *A&A*, **534**, A58
- Peres-Neto, P. R., Jackson, D. A., & Somers, K. M. 2005, *Computational Statistics and Data Analysis*, **49**, 974
- Petit, P., Donati, J.-F., Aurière, M., et al. 2005, *MNRAS*, **361**, 837
- Pettersen, B. R. 1980, *AJ*, **85**, 871
- Pillitteri, I., Maggio, A., Micela, G., et al. 2015, *ApJ*, **805**, 52
- Pillitteri, I., Wolk, S. J., Sciortino, S., & Antoci, V. 2014, *A&A*, **567**, A128
- Pizzolato, N., Maggio, A., Micela, G., Sciortino, S., & Ventura, P. 2003, *A&A*, **397**, 147
- Poppenhaeger, K., Robrade, J., & Schmitt, J. H. M. M. 2010, *A&A*, **515**, A98
- Poppenhaeger, K., & Schmitt, J. H. M. M. 2011, *ApJ*, **735**, 59
- Poppenhaeger, K., & Wolk, S. J. 2014, *A&A*, **565**, L1
- Queloz, D., Mayor, M., Weber, L., et al. 1999, arXiv:astro-ph/9910223
- Rahmati, A., Cravens, T. E., Nagy, A. F., et al. 2014, *GeoRL*, **41**, 4812
- Ramírez, I., Yong, D., Gutiérrez, E., et al. 2017, *ApJ*, **850**, 80
- Rauer, H., Catala, C., Aerts, C., et al. 2014, *ExA*, **38**, 249
- Reddy, A. B. S., & Lambert, D. L. 2017, *ApJ*, **845**, 151
- Redfield, S., & Linsky, J. L. 2004, *ApJ*, **602**, 776
- Ribas, I., Bolmont, E., Selsis, F., et al. 2016, *A&A*, **596**, A111
- Ribas, I., Guinan, E. F., Güdel, M., & Audard, M. 2005, *ApJ*, **622**, 680
- Rice, J. B., & Strassmeier, K. G. 2001, *A&A*, **377**, 264
- Rich, E. A., Wisniewski, J. P., McElwain, M. W., et al. 2017, *MNRAS*, **472**, 1736
- Rivera, E. J., Butler, R. P., Vogt, S. S., et al. 2010, *ApJ*, **708**, 1492
- Roberge, A. & Luvoir Mission Concept Team 2017, *LPICo*, **2042**, 4065

- Robertson, P., Endl, M., Cochran, W. D., et al. 2012, *ApJ*, 749, 39
- Rogers, T. M. 2017, *NatAs*, 1, 0131
- Saar, S. H., & Osten, R. A. 1997, *MNRAS*, 284, 803
- Sanchis-Ojeda, R., & Winn, J. N. 2011, *ApJ*, 743, 61
- Santos, N. C., Bouchy, F., Mayor, M., et al. 2004, *A&A*, 426, L19
- Santos, N. C., Mayor, M., Naef, D., et al. 2001, *A&A*, 379, 999
- Sanz-Forcada, J., Micela, G., Ribas, I., et al. 2011, *A&A*, 532, A6
- Schneider, A. C., & Shkolnik, E. L. 2018, *AJ*, 155, 122
- Schuler, S. C., Flateau, D., Cunha, K., et al. 2011, *ApJ*, 732, 55
- Schwarz, G. 1978, *AnSta*, 6, 461
- See, V., Jardine, M., Vidotto, A. A., BCOol Collaboration, et al. 2017, *MNRAS*, 466, 1542
- Ségransan, D., Mayor, M., Udry, S., et al. 2011, *A&A*, 535, A54
- Ségransan, D., Udry, S., Mayor, M., et al. 2010, *A&A*, 511, A45
- Segura, A., Walkowicz, L. M., Meadows, V., Kasting, J., & Hawley, S. 2010, *AsBio*, 10, 751
- Shields, A. L., Ballard, S., & Johnson, J. A. 2016, *PhR*, 663, 1
- Shkolnik, E., Walker, G. A. H., & Bohlender, D. A. 2003, *ApJ*, 597, 1092
- Shkolnik, E., Walker, G. A. H., Bohlender, D. A., Gu, P.-G., & Kürster, M. 2005, *ApJ*, 622, 1075
- Shkolnik, E. L., & Barman, T. S. 2014, *AJ*, 148, 64
- Shkolnik, E. L., & Llama, J. 2017, in *Handbook of Exoplanets*, ed. H. J. Deeg & J. A. Belmonte (Springer), 20
- Snellen, I., de Kok, R., Birkby, J. L., et al. 2015, *A&A*, 576, A59
- Spake, J. J., Sing, D. K., Evans, T. M., et al. 2018, *Natur*, 557, 68
- Stepien, K. 1988, *ApJ*, 335, 892
- Sullivan, P. W., Winn, J. N., Berta-Thompson, Z. K., et al. 2015, *ApJ*, 809, 77
- Tamaz, O., Ségransan, D., Udry, S., et al. 2008, *A&A*, 480, L33
- Terrien, R. C., Mahadevan, S., Deshpande, R., & Bender, C. F. 2015, *ApJS*, 220, 16
- Tian, F. 2015, *E&PSL*, 432, 126
- Tian, F., Kasting, J. F., Liu, H.-L., & Roble, R. G. 2008, *JGRE*, 113, 5008
- Tilley, M. A., Segura, A., Meadows, V. S., Hawley, S., & Davenport, J. 2017, arXiv:1711.08484
- Tinney, C. G., Butler, R. P., Marcy, G. W., et al. 2005, *ApJ*, 623, 1171
- Toner, C. G., & Gray, D. F. 1988, *ApJ*, 334, 1008
- Torres, G., & Ribas, I. 2002, *ApJ*, 567, 1140
- Tuomi, M., Jones, H. R. A., Barnes, J. R., Anglada-Escudé, G., & Jenkins, J. S. 2014, *MNRAS*, 441, 1545
- Tuomi, M., Jones, H. R. A., Jenkins, J. S., et al. 2013, *A&A*, 551, A79
- Turner, J. D., Christie, D., Arras, P., Johnson, R. E., & Schmidt, C. 2016a, *MNRAS*, 458, 3880
- Turner, J. D., Pearson, K. A., Biddle, L. I., et al. 2016b, *MNRAS*, 459, 789
- Valenti, J. A., & Fischer, D. A. 2005, *ApJS*, 159, 141
- Vidal-Madjar, A., Lecavelier des Etangs, A., Désert, J.-M., et al. 2003, *Natur*, 422, 143
- Vidotto, A. A., Fares, R., Jardine, M., et al. 2012, *MNRAS*, 423, 3285
- Vidotto, A. A., Jardine, M., & Helling, C. 2010, *ApJL*, 722, L168
- Vogt, S. S., Butler, R. P., Marcy, G. W., et al. 2005, *ApJ*, 632, 638
- von Braun, K., Boyajian, T. S., ten Brummelaar, T. A., et al. 2011, *ApJ*, 740, 49
- Wheatley, P. J., Louden, T., Bourrier, V., Ehrenreich, D., & Gillon, M. 2017, *MNRAS*, 465, L74
- Wittrock, J. M., Kane, S. R., Horch, E. P., et al. 2017, *AJ*, 154, 184
- Wood, B. E., Laming, J. M., & Karovska, M. 2012, *ApJ*, 753, 76
- Wood, B. E., Redfield, S., Linsky, J. L., Müller, H.-R., & Zank, G. P. 2005, *ApJS*, 159, 118
- Woods, T. N., Chamberlin, P. C., Harder, J. W., et al. 2009, *GeoRL*, 36, 1101
- Wolf, V. M., & Wallerstein, G. 2005, *MNRAS*, 356, 963
- Wright, J. T., Marcy, G. W., Butler, R. P., et al. 2008, *ApJL*, 683, L63
- Wright, J. T., Marcy, G. W., Butler, R. P., & Vogt, S. S. 2004, *ApJS*, 152, 261
- Yelle, R. V. 2004, *Icar*, 170, 167
- Yıldız, M., Çelik Orhan, Z., & Kayhan, C. 2016, *MNRAS*, 462, 1577
- Youngblood, A., France, K., Loyd, R. O. P., et al. 2016, *ApJ*, 824, 101
- Zahn, J.-P. 2008, in *EAS Publications Ser. 29*, ed. M.-J. Goupil & J.-P. Zahn, 67
- Zarka, P. 2007, *P&SS*, 55, 598
- Zhang, L. 2011, in *ASP Conf. Ser. 451*, 9th Pacific Rim Conference on Stellar Astrophysics, ed. S. Qain et al. (San Francisco, CA: ASP), 123
- Zhao, L., Fischer, D. A., Brewer, J., Giguere, M., & Rojas-Ayala, B. 2018, *AJ*, 155, 24